Ph.D. DISSERTATION

Robotic Finger Design with Human Musculoskeletal Characteristics

사람 근골격 특성을 반영한 로봇 손가락 설계

BY

SEUNGYEON KIM

FEBRUARY 2023

DEPARTMENT OF TRANSDISCIPLINARY STUDIES
THE GRADUATE SCHOOL OF CONVERGENCE
SCIENCE AND TECHNOLOGY
SEOUL NATIONAL UNIVERSITY

Robotic Finger Design with Human Musculoskeletal Characteristics

사람 근골격 특성을 반영한 로봇 손가락 설계

지도교수 박 재 홍

이 논문을 공학박사 학위논문으로 제출함

2023년 1월

서울대학교 대학원

융합과학부

김 승 연

김승연의 공학박사 학위 논문을 인준함

2023년 1월

위 원 장   전 동 석   (인)
부위원장   박 재 홍   (인)
위   원   배 지 훈   (인)
위   원   박 용 래   (인)
위   원   김 의 겸   (인)

Abstract

What the manipulator can perform is determined by what the end-effectors, including the robotic hand, can do because it is the gateway that directly interacts with the surrounding environment or objects. In order for robots to have human-level task performance in a human-centered environment, the robotic hand with human-hand-level capabilities is essential. Here, the human-hand-level capabilities include not only force-speed, and dexterity, but also size and weight. However, to our knowledge, no robotic hand exists that simultaneously realizes the weight, size, force, and dexterity of the human hand and continues to remain a challenge. In this thesis, to improve the performance of the robotic hand, the modular robotic finger design with three novel mechanisms based on the musculoskeletal characteristics of the human hand was proposed.

First, the tendon-driven robotic finger with intrinsic/extrinsic actuator arrangement like the muscle arrangement of the human hand was proposed and analyzed. The robotic finger consists of five different tendons and ligaments. By analyzing the fingertip speed while a human is performing various object grasping motions, the actuators of the robotic finger were separated into intrinsic actuators responsible for slow motion and an extrinsic actuator that performs the motions requiring both large force and high speed.

Second, elastomeric continuously variable transmission (ElaCVT), a new concept relating to continuously variable transmission (CVT), was designed to improve the performance of the electric motors remaining weight and size and applied as an extrinsic actuator of the robotic finger. The primary purpose of ElaCVT is to expand the operating region of a twisted string actuator (TSA)

and duplicate the force-velocity curve of the muscles by passively changing the reduction ratio according to the external load applied to the end of the TSA. A combination of ElaCVT and TSA (ElaCVT-TSA) is proposed as a linear actuator. With ElaCVT-TSA, an expansion of the operating region of electric motors to the operating region of the muscles was experimentally demonstrated.

Finally, as the flexion/extension joints of the robotic finger, anthropomorphic rolling contact joint, which mimicked the structures of the human finger joint like tongue-and-groove, and collateral ligaments, was proposed. As compliant joints not only compensate for the lack of actuated degrees of freedom of an under-actuated system and improve grasp stability but also prevent system failure from unexpected contacts, various types of compliant joints have been applied to end-effectors. Although joint compliance increases the success rate of power grasping, when the finger wraps around large objects, it can reduce the grasping success rate in pinch gripping when dealing with small objects using the fingertips. To overcome this drawback, anthropomorphic rolling contact joint is designed to passively adjust the torsional stiffness according to the joint angle without additional weight and space. With the anthropomorphic rolling contact joint, the stability of pinch grasping improved.

keywords: Robotic hand, Continuously variable transmission, Compliant joint, Biomimetics

student number: 2015-26106

Contents

List of Tables

List of Figures

Chapter 1

INTRODUCTION

1.1 MOTIVATION: ROBOTIC HANDS

The human hand and wrist consist of 27 bones and 27 joints, and are actuated by 34 muscles. Human hands can exert fingertip force over 30 N, and the maximum joint velocity exceeds 400 deg/s [1]. What's even more surprising is that the total volume and the weight of the hand and forearm that implements all these features are only about 0.15 m^2 and 1.5 kg [2][3]. For these reasons, the human hand has been considered to be the most dexterous end-effector until now, and designing a robotic hand that achieves the performance of human hand remains challenging. In order for manipulators, including humanoid robots, to perform various tasks like humans in a human-centered environment, a human-hand level end-effector is essential. Various characteristics of human hands have been studied to improve the performance of robotic hands, and various structures and mechanisms have been developed. Each robotic hand has unique characteristics based on its own design goals. However, due to the common goal of reproducing

the structure and the performance of a human hand, there were types, locations, and the number of actuators that are widely used when designing robotic hands. The actuator types can be classified into the electric motor, linear actuator using ball screw, linear actuator with tendons, and pneumatic actuator. Depending on the actuation types and the structure of the robotic hands, the actuators could be located inside the hand or outside the system. The number of actuators varies greatly depending on the design goal of the robotic hand. Each mechanism has strengths and limitations.

The direct-driven system using electric motors is the most easily found actuation type of robotic system including robotic hands. With this actuation system, joints are directly connected to the actuator without bulky transmissions like linkage or ball screws. Since the joints and the actuators correspond one-to-one, not only does the mechanical structure of the robotic hand become simplified, but also the complexity of the control algorithm can be reduced. Due to the low complexity, these robotic hands have the advantage of higher system reliability and durability than others. In addition, since all actuators are included inside the hand, it has the advantage of being easily integrated into the existing manipulator without developing customized manipulators.

KITECH hand developed by Lee et al. is a fully actuated robotic hand with four modular robotic fingers. Each finger has four joints like a human finger which are actuated by different four actuators. KITECH hand not only realizes high dexterity but also expands the dexterity of the robotic hand by adjusting one of the joint directions of the metacarpophalangeal joint [4]. Similarly, MPL v2.0 , designed by Matthew S. Johannes et al. is one of a robotic hand using direct drive. Unlike KITECH hand, MPL v2.0 used 12 small actuators and cou-

pling mechanisms inside the hand to realize human-level dexterity [5]. Instead of using more actuators, MPL V2.0 integrated more than 100 sensors including force, position, and temperature sensors inside the hand.

Human joints are actuated by the linear motion of muscles. Based on this musculoskeletal characteristic, various robotic hands using linear actuators have also been developed. Linear actuators applied to robotic hands can be largely classified into two different types, one converting rotational motion into linear motion using a ball screw or lead screw with linkages and the other transmitting power using a tendon, which is called tendon-driven mechanism. Due to the different characteristics of these two, robotic hands using different linear actuators have completely different strengths and limitations.

ILDA hand, developed by Kim et al. proposed a five-finger robot hand based on a modular finger in which four finger joints are actuated by three actuators. All linear actuators were placed under the palm and torque was transmitted to each joint through rigid linkages. ILDA hand showed that not only it can exert great fingertip force, but also it is possible to use delicate tools including tweezers and scissors by utilizing the force/torque sensor integrated into the fingertip [6]. Schunk SVH 5-finger hand developed by Schunk Corporation designed coupling mechanisms between joints based on the motion characteristics of human hand joints. SVH 5-finger hand used 8 actuators to drive 20 joints [7].

Unlike the ILDA hand and Schunk SVH 5-finger hand, which tried to increase dexterity by using a linear actuator and joint coupling mechanism, the robotic hands for prosthetic hands abandoned high dexterity by using a small number of linear actuators with a high reduction ratio, to achieve a light and

compact structure with strong grasping force to perform various tasks of daily life, firmly. Bebionic hand and i-limb have 10 joints but are driven by only 5 and 6 actuators, respectively. However, i-limb includes a carpometacarpal adduction/abduction joint actuator for thumb opposition, but Bebionic hand implements thumb opposition through a passive mechanism [8][9][10]. One of the limitations of robotic hands for prosthetics is that actuators and mechanisms must be implemented in the volume of the human hand. When using multiple actuators to achieve high dexterity, the size of each actuator is inevitably reduced, and on the contrary, when a relatively bulky actuator is used for a large force, dexterity is inevitably abandoned.

Robotic hands using linear actuators with tendons include the Dexterous hand, Dexmart hand, Fllex hand, Robonaut 2 hand, and DLR Hand Arm system. These robotic hands commonly implemented high dexterity and grasp force by using more than 20 joints and 15 actuators. Also, all actuators are mounted in the space of the lower arm to reduce the size of the hand. Using 20 actuators, Dexterous hand developed by Shadow robotics actuated 24 joints including 2 dofs wrist joints and one additional palm joint [11]. Dexmart hand use 24 twisted string actuators integrated with 1 degree of freedom force sensor [12]. In the Fllex hand developed by Kim et al., 3 actuators, 15 in total, were used to actuate each finger, and to the efficiency of the tendon-driven mechanism, a novel lubrication structure was introduced [13]. DLR Hand ARM system used 42 actuators to drive 21 degrees of freedom including the wrist joints. Each joint was driven antagonistically by two actuators, enabling active joint stiffness control which is one of the human musculoskeletal characteristics [14]. However, due to the large size and heavy weight of the lower arm (4.3 kg of Dexterous hand, 4.5 kg DLR Hand Arm system), it is difficult to use these

tendon-driven robotic hands as an end effector of commercial manipulators. In addition, the efficiency is reduced by the friction generated in the power transmission process, and the high complexity of the system due to the design of the tendon path makes fabrication and maintenance difficult.

Unlike dexterous tendon-driven robotic hands, compact-size robotic hands that locate all tendon-driven actuators inside the hand also have been developed. These robotic hands utilized the flexibility of the tendon to implement the musculoskeletal characteristics of the human hand within a compact system size, but due to the limited size, the degree of freedom was reduced or actuators with limited power capacity had to be used [15][16][17].

Recently, robotic hands and grippers using pneumatic actuators have been applied to various industrial fields. Due to the flexibility of the soft material, the soft grippers and soft robotic hands have the following two advantages. First, it improves the durability of the system by absorbing the shock that can occur between the gripper and the object. The ability to flexibly deal with collisions is an advantage for grippers which frequently perform direct contact. In particular, grippers and robotic hands used in the human-centered environment must be able to deal with unexpected collisions. The second advantage is that the shape of the robotic hands can adapt and change according to the shape of the grasped object, so it can stably grasp the object without a complex grasping algorithm. Due to the robustness against impact and adaptability to various shapes, systems with soft robotic hands are widely applied to industrial fields such as product sorting automation that must respond to various objects.

Feng et al. proposed a soft robotic hand that is controlled using surface electromyography signals. Each finger has three independent degrees of free-
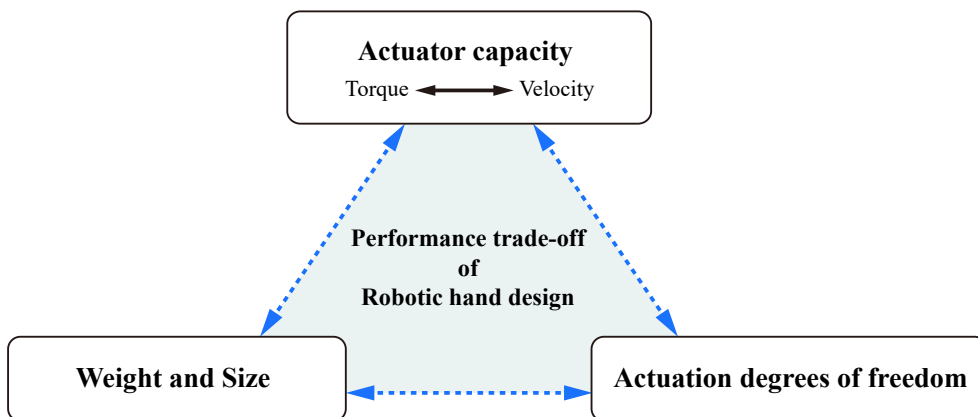
Figure 1.1: Performance trade-off relationship of designing robotic hand. Actuator capacity, Weight and size and Actuation degrees of freedom are representative performances when evaluate the robotic hands. Under this trade-off relationship the robotic hand cannot achieve all three human hand level performances.

dom for flexion/extension, and various grasping postures were demonstrated by optimizing the length and shape of the pneumatic actuator [18]. BCL-26, developed by Zhou et al, had 26 joints and is actuated by 22 pneumatic actuators, which implemented human-level dexterity. A novel x-chamber soft actuator was applied to the metacarpophalangeal adduction/abduction joint to expand the workspace of the fingers [19]. RBO hand2 used only one pneumatic actuator for each finger but designed two additional degrees of freedom on the palm to improve dexterity. Abondance et al. designed modular fingers with two degrees of freedom, and proposed a four-finger soft robotic hand that perform translational and rotational in-hand manipulation for objects of various sizes [20][21]. However, the pneumatic pump that actuates the soft robotic hand has a structure that is difficult to be integrated into the hand or lower arm. This not only increases the size and weight of the overall system but also increases the complexity of the system.

Table 1.1 shows the characteristics, strengths, and limitations of the afore-mentioned robotic hands, including the type of actuator and the position of the actuator. As a result, no robot hand that simultaneously implements all the characteristics of a human hand has been developed until now. This is because the robot hand design has a trade-off relationship between the required performance values as shown in Fig.1.1. Actuator capacity, degree of freedom, and weight and size of the robot hand are the three most important performances. This trade-off relationship means that if you improve the performance of two of the three performance indicators, the performance of the other one on the other side will necessarily deteriorate. For example, if an actuator is added to increase the degree of freedom(dexterity) maintaining the performance of each actuator, increases in weight and size of the robotic hand must not be avoided like Dexterous hand. On the contrary, in order to maintain the size and weight of a human hand and implement a strong grasping force like Bebionic hand, it is inevitable to have a low degree of freedom. Therefore, in order to increase the overall performance of the robotic hand under this trade-off relationship, it is necessary to maximize the advantages of each system while improving the disadvantages.

Table 1.1: Characteristics of robotics hands

Name	Joint #	Actuator #	Finger #	Weight	Actuator type	Actuator position	Strengths	Limitations	Characteristics
MPL hand v2 [5]	20*	12*	5	1.315 kg*	Electric motor	Inside hand	-	Low dexterity	Dexterous thumb (4 active degrees of freedom), over 100 integrated sensors including torque, force, contact, and temperature sensors
KITECH hand [4]	16	16	4	1.09 kg			High dexterity	Limited size of actuators	Different MCP AA joint direction from human, modular finger structure
ILDA hand [6]	20	15	5	1.1 kg					Fingertip PF sensor, modular finger structure, high degree of freedom and strong grasping force
SVH 5-finger hand [7]	20	9	5	1.3 kg	Linear*		-	High complexity	The size of a human hand, the difference in the number of actuators for each finger (two actuators for thumb, index, middle finger, and one actuator for ring, small finger)
i-limb [8][10]	10	6	5	0.528 kg		Human hand size	Strong grasping force*	Low dexterity	Prosthetic hand which has a active CMC joint for thumb opposition
Bebionic hand [8][9]	10	5	5	0.616 kg					Prosthetic hand which has a passive CMC joint for thumb opposition
DLR hand 2 [15]	17	13	4	1.8 kg	Linear** + Electric motor		High dexterity	Heavy weight	Direct driven for MCP joints, tendon driven for PIP and DIP joints
iit soft hand 2 [16]	19	2	5	-			Large size actuator, Strong grasping force	Extremely low dexterity	Realization of kinematic synergy with only two actuators based on object grasping postures
aku hand V [17]	18	14	4	0.825 kg			High dexterity	-	Inter-Metacarpal joint implementation to expand finger workspace
iCub hand [22]	12	8	5	-	Linear**	In/outside hand	-	Low dexterity	Two actuators located inside the hand (thumb opposition, MCP joint adduction/abduction), six actuators located on the lower arm
Shadow Dexterous hand [11]	24*	20*	5	4.3 kg*		Outside hand	-	High complexity, Difficult maintenance	Implementation of human hand size and degrees of freedom with additional degrees of freedom in the palm
Dexmart hand [12]	22*	24*	5	-		High dexterity			Actuated by using a twisted string actuator integrated with a 1-degree-of-freedom force sensor
Robonaut 2 hand [23]	23*	19*	5	-					Difference in the number of actuators for each finger (4 actuators for the index and middle fingers, 2 actuators for the ring and small fingers, 5 actuators for the thumb)
DLR Hand Arm system [14]	20	44	5	4.5 kg*			Heavy weight		Actuators are driven antagonistically for all joints and joint stiffness can be actively adjusted
FLEX hand [13]	20	15	5	2.27 kg*					Reduce internal friction by applying flexible rolling contact joint and lubrication structure
Soft robotic hand [18]	15**	15	5	-			Impact absorber		Independent control of the three flexion/extension joints of each finger
BCL-26 [19]	26**	22	5	-	Pneumatic pump			Low control precision	Additional degrees of freedom in axial extension
RBO Hand2 [20]	7**	7	5	0.178 kg**			-		Improved dexterity by placing two actuators on the palm by applying x-chamber soft actuator structure to MCP adduction/abduction joint
Dexterous soft robotic hand [21]	8**	8	4	-			*Mechanical locking mechanism		4-finger soft robotic hand in the form of a gripper, implementation of in-hand manipulation

* Including wrist
** Continuum

* Including wrist

* Including wrist
** Without actuators

*Ball screw + electric motor
***Tendon driven
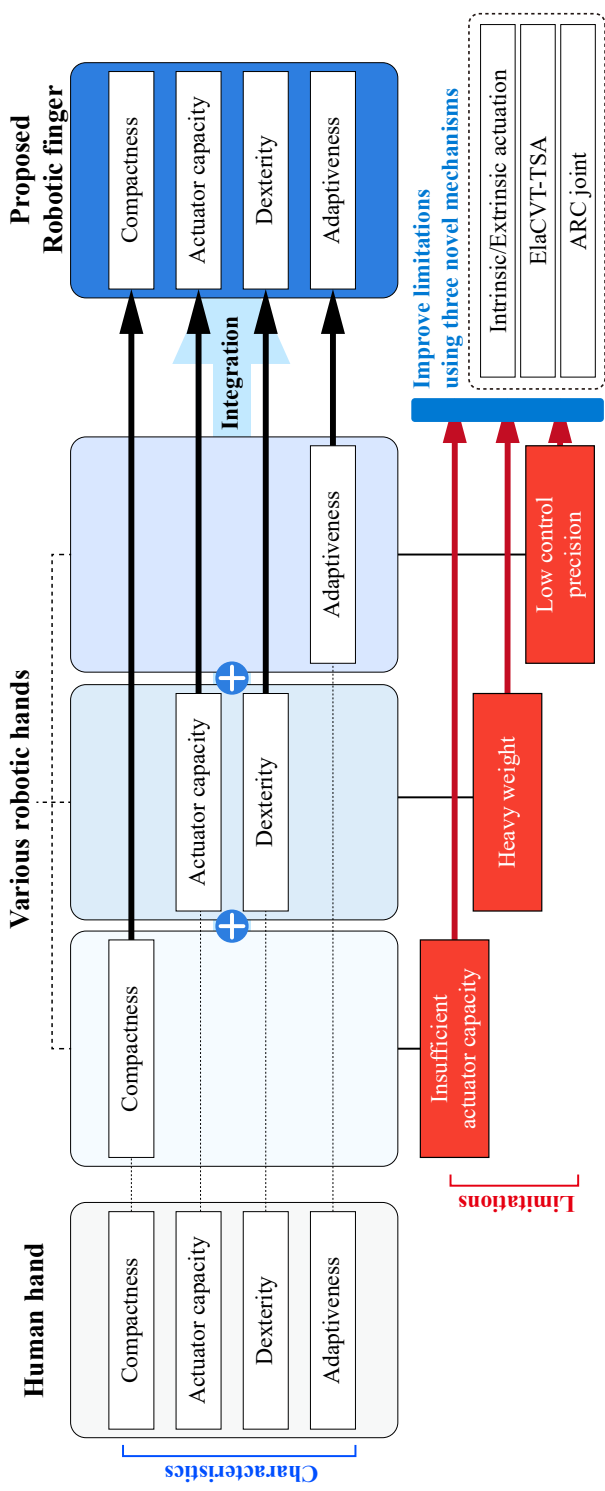
Figure 1.2: Characteristics of humand and three different robotic hands.

9
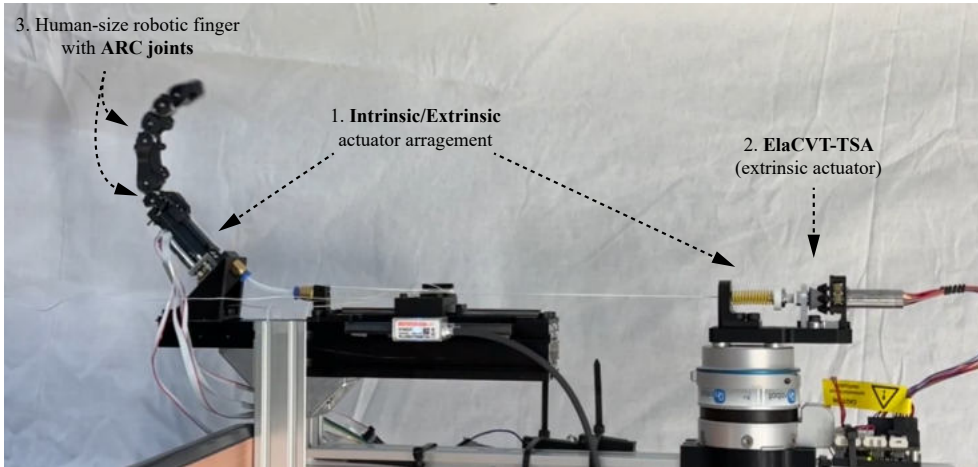
Figure 1.3: Robotic finger system

1.2 CONTRIBUTIONS OF THESIS

In this study, a novel tendon-driven robotic finger structure is proposed to improve the limitations of various robotic hands including insufficient actuator capacity, heavyweight, and low control precision which are essential abilities for realizing human hand-level performance, and Fig. 1.2 shows the overall contribution of the study. Various robotic hands have strengths depending on the design purpose, but also have limitations compared to the human hand. To improve the limitations of each robotic hand and integrate the strengths of various robotic hands into one unified robotic finger, the robotic finger design with three novel mechanisms based on the musculoskeletal characteristics of the human hand is proposed. The proposed robotic finger was designed considering the size and weight of the human hand, as well as the degrees of freedom, strength, and joint velocity. Three mechanisms based on human musculoskeletal characteristics, *intrinsic/extrinsic actuator arrangement, elastomeric continuously variable transmission combined with twisted string actuator (ElaCVT-TSA),*

and *anthropomorphic rolling contact joint (ARC joint)*, were proposed and integrated as shown in Fig. 1.3.

1.2.1 Intrinsic/Extrinsic Actuator arrangement

The actuator system with tendons increases the complexity of the system and manufacturing difficulty, but has the advantage of being applicable to various new mechanisms due to the flexibility of tendons. The first contribution of the finger is that, in the human hand, muscles related to hand motion are divided into intrinsic muscles which are located inside the hand, and extrinsic muscles which are located in the lower arm. By analyzing the fingertip velocity of the index finger of a human while grasping various objects, a tendon-driven robotic finger structure is proposed where the intrinsic actuators are responsible for slow motion and an extrinsic actuator performs the motions that require both large force and fast joint velocity. With this separated actuator arrangement, the proposed robotic finger has a more balanced shape through the optimized selection and arrangement of actuators.

1.2.2 Linear actuator mimicking human muscle properties

Second, to mimic the characteristics of muscles, Elastomeric continuously variable transmission (ElaCVT), a new concept relating to continuously variable transmission (CVT), is designed to improve the performance of the extrinsic actuator. The primary purpose of ElaCVT is to expand the operating region of a twisted string actuator (TSA) and duplicate the force-velocity curve of the muscles by passively changing the reduction ratio according to the external load applied to the end of the TSA. A combination of ElaCVT and TSA

(ElaCVT-TSA) is proposed as a linear actuator that The deformation of *elastomer* changes the reduction ratio without the need for complicated mechanisms.

1.2.3   Flexible rolling contact joint

Third, a novel compliant rolling contact joint, *anthropomorphic rolling contact joint*, that mimicked the structures of the human finger joint, tongue-and-groove, and collateral ligaments is proposed. Although joint compliance increases the success rate of power grasping, when the finger wraps around large objects, it can reduce the grasping success rate in pinch gripping when dealing with small objects using the fingertips. To overcome this drawback, anthropomorphic rolling contact joint is designed to passively adjust the torsional stiffness according to the joint angle without additional weight and space.

Chapter 2

ROBOTIC FINGER STRUCTURE WITH HUMAN-LIKE ACTUATOR ARRANGEMENT

The joints of a human are generally actuated by the motion of multiple muscles, and there is a difference in the number of muscles passing around the different joints. Six muscles related to finger movement pass around the metacarpal joint, but only two tendons are connected to the distal interphalangeal joint, which exists in the most distal position because the muscles of the finger are located in the palm and forearm structure of the finger. Due to the complex tendon arrangement of the human finger and the difference in the characteristics of each muscle, there is a difference in strength and velocity of the fingertip depending on the posture and motion direction of the fingertip.

In this chapter, the characteristic of fingertip velocity when grasping objects in daily life was analyzed, and a tendon-driven robotic finger with a human-like actuator arrangement was proposed. The proposed tendon structure consists of two types of tendons divided into tendons responsible for relatively slow
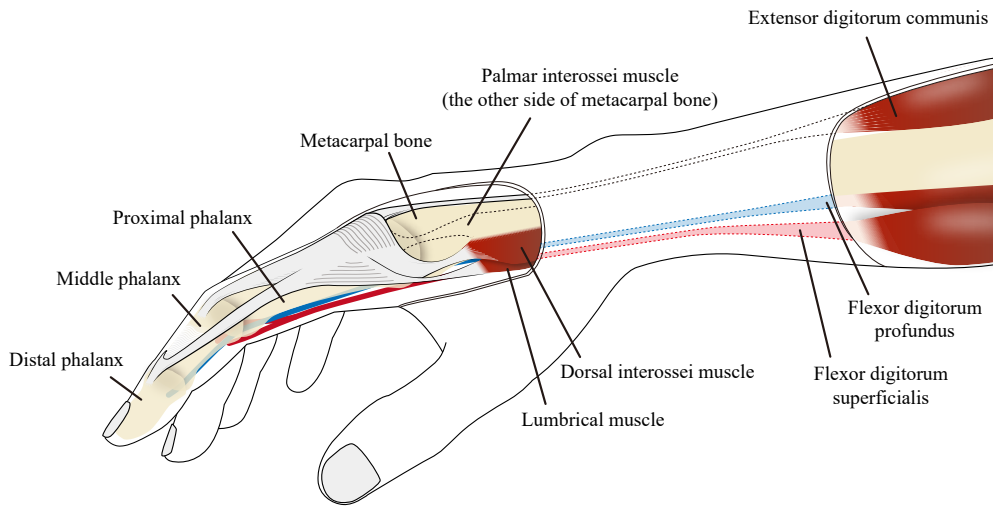
Figure 2.1: Anatomy of index finger which is actuated by three intrinsic muscles (lumbrical, dorsal interossei, palmar interossei muscles) and three extrinsic muscles (flexor digitorum profundus, flexor digitorum superficialis, extensor digitorum communis)

contraction speed and tendons that requires fast contraction speed. To solve the problem of tendon-driven fingers, that the increase in size and weight of the forearm due to multiple actuators, the proposed robotic finger has intrinsic actuators placed inside of the hand and an extrinsic actuator placed outside of the hand, separately.

2.1   ANALYSIS OF HUMAN FINGERTIP VELOCITY

Fig. 2.1 shows the anatomy of the human index finger. The index finger consists of four bones, metacarpal bone, proximal phalanx, middle phalanx, and distal phalanx, and four joints, flexion/extension (FE) and adduction/abduction (AA)

of metacarpophalangeal (MCP) joint, FE of proximal interphalangeal (PIP) joint, and FE of distal interphalangeal (DIP) joint. And, the six muscles, which actuate four joints, are the flexor digitorum profundus (FDS), flexor digitorum superficialis (FDS), extensor digitorum communis (EDC), dorsal interossei (DI), palmar interossei (PI), and lumbrical (LUM) [24]. The six muscles have different muscle characteristics, including maximum contraction force, contraction velocity, nominal length, etc., and are classified into intrinsic muscles and extrinsic muscles. Intrinsic muscles are located inside the hand, and extrinsic muscles are located in the forearm according to the location of origin. As illustrated in Fig. 2.1, FDS, FDP, and EDC are extrinsic muscles whose muscles originate from the forearm [25]. In contrast, DI, PI, and LUM are intrinsic muscles whose origins are located inside the hand. Compared to intrinsic muscles, extrinsic muscles have a relatively large cross-sectional area and long fiber length, so they can produce large forces and high contraction speeds [26][27][28].

As intrinsic muscles and extrinsic muscles have different characteristics and the difference in the moment arm for the joints, it is known that each muscle are responsible for different finger motions [29][30]. Extrinsic muscles are known to be responsible for large hand movements. The reason is that the extrinsic muscles actuate the flexion joints of the fingers in the same direction. FDS generate the flexion motion of MCP and PIP joints, and FDP is responsible for flexion of MCP, PIP and DIP joints. And EDC generate extension motion of MCP, PIP joint and DIP joint at the same time. Conversely, the intrinsic muscles have moment arms in opposite directions according to the joints. For example, when the lumbrical contracts, the MCP joint flexes but the PIP extends. Because of these properties, intrinsic muscles allow the fingers to perform fine movements
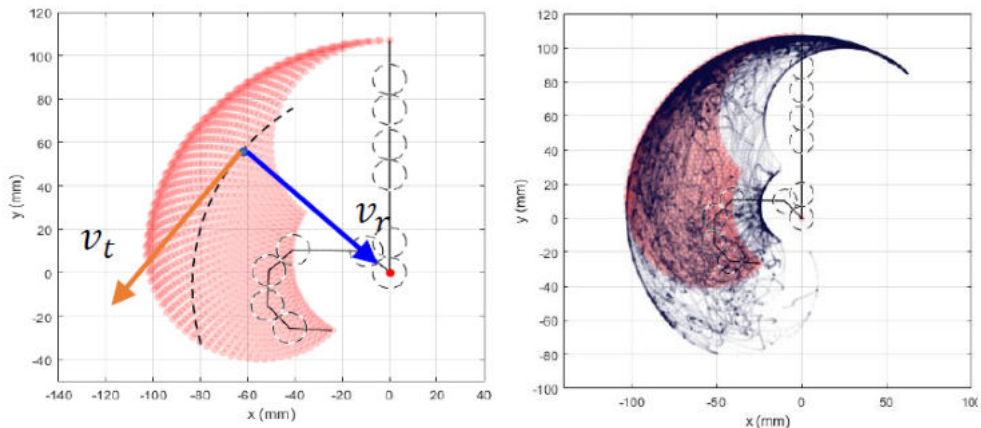
Figure 2.2: (a) Fingertip velocity decomposed in polar coordinates, (b) Hitmap of fingertip position of the index finger using UNIPI dataset

The velocity of the fingertip according to the direction was analyzed based on the musculoskeletal characteristic of the hand that the intrinsic and extrinsic muscles are responsible for different movements. The UNIPI dataset (August 2018) proposed by Santian et al. was used [31] to evaluate fingertip velocity when grasping daily life objects. In this dataset, the 20 joint angles when grasping 21 objects performed by 6 subjects were recorded. The subject repeated the motion of approaching and holding the target object twice in the preparation posture without any additional restrictions. The fingertip velocity was calculated using index finger joint value data from UNIPI dataset and the kinematic of the finger model. Fingertip velocity was analyzed by decomposing it into tangential velocity (v_t) and central velocity (v_r) using polar coordinates based on the center of the MPC joint. Fig. 2.2(a) shows the decomposed fingertip velocity and Fig. 2.2(b) shows the fingertip positions of all subjects' index fingers in UNIPI dataset with navy points. In Fig. 2.2(b), the more frequently the fingertips were located, the darker the points were.

For the grasping motion of 21 objects in UNIPI dataset, the average value
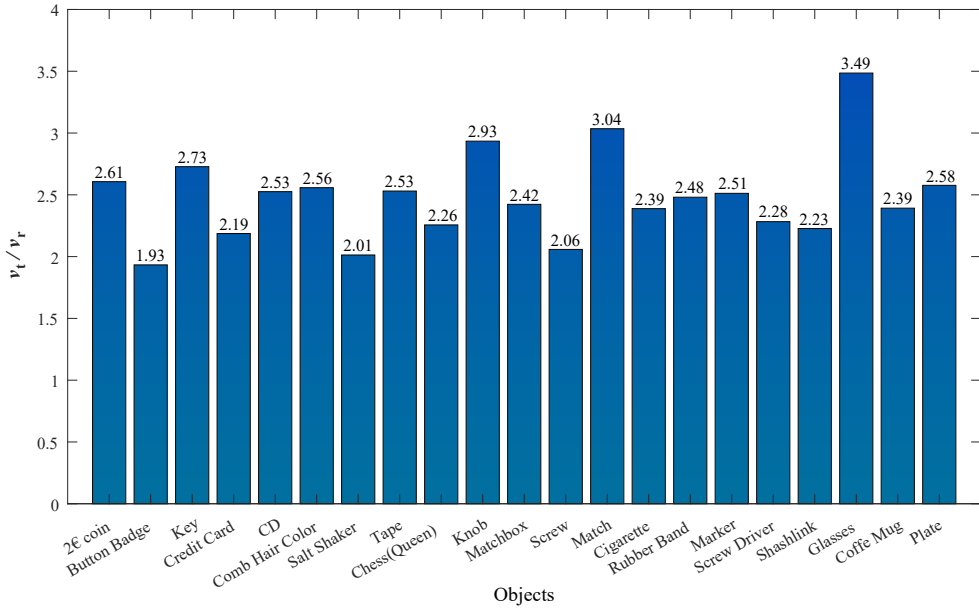
Figure 2.3: (a) Fingertip velocity decomposed in polar coordinates, (b) Hitmap of fingertip position of the index finger using UNIPI dataset

of v_t is 2.48 times that of v_r. Fig. 2.3 shows the velocity ratio that v_t divided by v_r. The largest differences between v_t and v_r were observed when holding thin and small objects such as glasses, matches, knobs, and keys. Even in the case of showing the smallest speed difference, grasping button badge, v_t was 1.9 times v_r. The results revealed that the velocity of the fingertip is not consistent across different directions during object grasping. This implies that the overall size and weight of the system can be reduced by utilizing a compact actuator with a high reduction ratio for the actuator responsible for relatively low-speed motion.

2.2 THE ROBOTIC FINGER WITH INTRINSIC/EXTRINSIC ACTUATORS

2.2.1 The structure of proposed robotic finger

Fig. 2.4(a) shows the kinematics diagram of the proposed robotic finger in the sagittal plane. The robot finger consists of four phalanges, metacarpal, proximal phalanx, middle phalanx, and distal phalanx, and four joints that are identical to the human finger. MCP joint has two degrees of freedom of AA (q_0) and FE (q_1), and PIP joint and DIP joint have one degree of freedom of FE (q_2 and q_3) respectively. Except for MCP AA joint, the three FE joints consist of anthropomorphic rolling contact joints (ARC joint), which are novel flexible joints discussed in Chapter 4, and MCP AA joint was a pin joint. The ARC joints were represented by pair of two gray cylinders with equal radii, and the contact points between two phalanges were depicted by orange points.

Most parts of the robotic finger consist of tough polylactide (PLA) and are manufactured using a 3D printer, Ultimaker S5, as shown in Fig. 2.4(b). Especially, by applying ARC joints to MCP FE, PIP FE, and DIP FE joints, the number of metal parts such as bearings could be reduced, and the total weight of the robotic finger including the two actuators was measured at 75 g. Considering that the average adult male hand weighs 500g, the proposed robotic finger's weight and size show the possibility of implementing a robotic hand equivalent to a human hand [2].

The overall length and width excluding the metacarpal bone of the robotic finger were 106 mm and 18 mm, respectively, and Fig. 2.4(c) shows that the
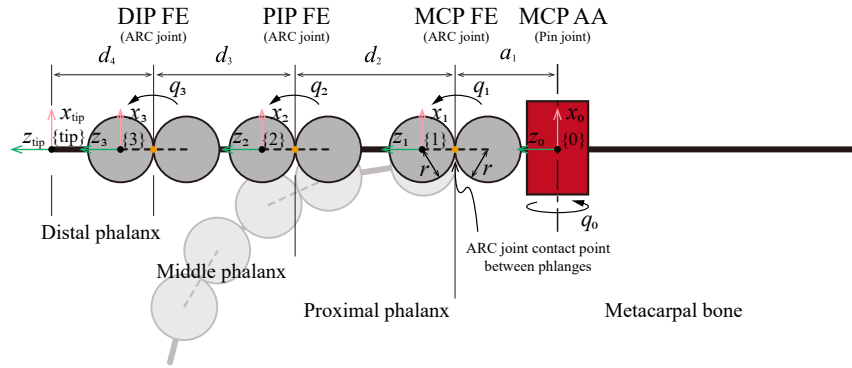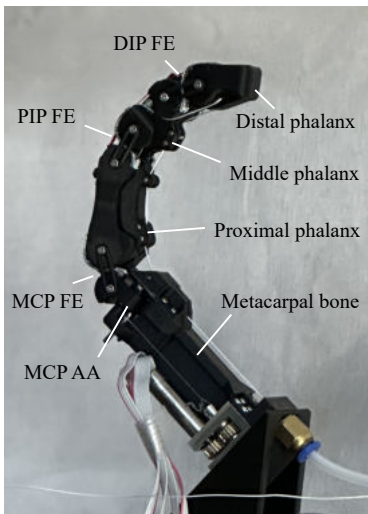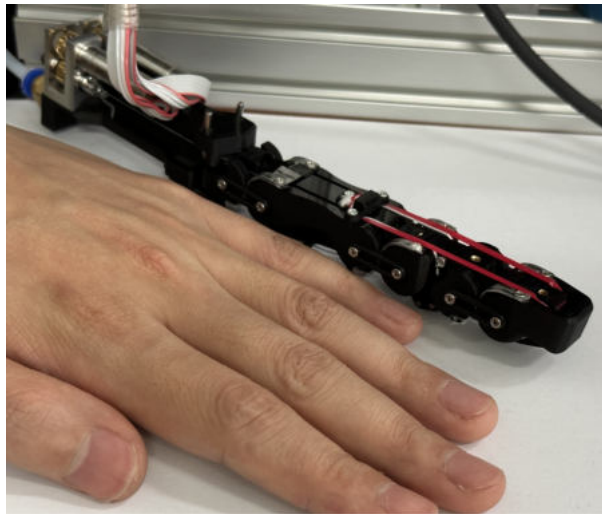
Figure 2.4: Proposed robotic finger, (a) Kinematic diagram of the robotic finger and parameter definitions, (b) Manufactured robotic finger, (c) Comparison of the size of the robotic finger and a human hand

Table 2.1: Phalange length of a human finger and proposed robotic finger.

Length (mm)	a_1	d_2	d_3	d_4	sum	ratio
Human finger	18	49.5	31.9	20	119.4	100%
Robotic finger	6	45	30	25	106	89%

Table 2.2: Range of motion of human finger and proposed robotic finger

Range of motion	MCP AA (q_0)	MCP FE (q_1)	PIP FE (q_2)	DIP FE (q_3)
Human finger	$\pm30°$	$0° \sim +90°$	$0° \sim +90°$	$0° \sim +90°$
Robotic finger	$\pm25°$	$0° \sim +90°$	$0° \sim +90°$	$0° \sim +90°$

robotic finger had similar length and width to those of the human hand. Table 2.1 shows the length of each phalanx of human and proposed robotic fingers defined in Fig. 2.4(a). The phalange length of the proposed robotic finger is measured in the fully extended posture, and a_1 represents the offset between the MCP AA joint rotation axis and the MCP FE joint rotation axis [32]. The length of the robot's finger is 89 percent of the length of a human finger. The length of the metacarpal bone where the two actuators were located was 80.5 mm.

2.2.2 Kinematics of the robotic finger

The fingertip position of the robotic finger with ARC joints is estimated using the same way as the robotic finger where the rolling contact joint is applied. Assuming that the radius of the rolling surfaces of the proximal and distal bodies of the rolling contact joints are equal to r, when the total joint angle of the rolling contact joint rotates by θ, the contact point between two bodies rotates a half of θ. Using the length and joint angle parameter expressed in Fig. 2.4(a), the position and rotation of each coordinate system of phalanges,

from $\{0\}$ to $\{3\}$ including fingertip, $\{tip\}$, are calculated as a multiplication of homogeneous transformation matrices as Equation (2.1) [33].

$$
\begin{aligned}
T_{01} =& Rot(\hat{x}, q_0) \\
T_{02} =& T_{01} * Trans(\hat{y}, a_1 - r) * Rot(\hat{z}, q_1/2) * Trans(\hat{y}, 2r) * Rot(\hat{z}, q_1/2) \\
T_{03} =& T_{02} * Trans(\hat{y}, d_2 - 2r) * Rot(\hat{z}, q_2/2) * Trans(\hat{y}, 2r) * Rot(\hat{z}, q_2/2) \\
T_{04} =& T_{03} * Trans(\hat{y}, d_3 - 2r) * Rot(\hat{z}, q_3/2) * Trans(\hat{y}, 2r) * Rot(\hat{z}, q_3/2) \\
T_{0tip} =& T_{04} * Trans(\hat{y}, d_4 - r)
\end{aligned}
$$

$$(2.1)$$

$Trans()$ and $Rot()$ are matrices representing linear and rotation displacement, respectively. The first element represents the direction of linear motion and rotation, and the second element represents the quantity as shown in Equation (2.2).
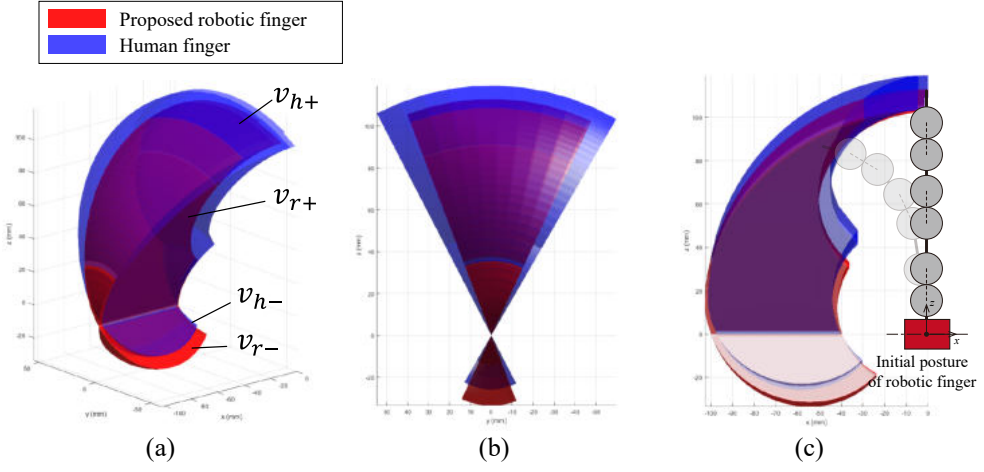
Figure 2.5: Workspace of the robotic finger (red) and human finger (blue). (a) Isometric view, (b) Front veiw, (c) Lateral veiw.

$$Rot(\hat{x}, \theta) = \begin{bmatrix} 1 & 0 & 0 & 0 \\ 0 & \cos(\theta) & -\sin(\theta) & 0 \\ 0 & \sin(\theta) & \cos(\theta) & 0 \\ 0 & 0 & 0 & 1 \end{bmatrix}$$

$$Rot(\hat{z}, \theta) = \begin{bmatrix} \cos(\theta) & -\sin(\theta) & 0 & 0 \\ \sin(\theta) & \cos(\theta) & 0 & 0 \\ 0 & 0 & 1 & 0 \\ 0 & 0 & 0 & 1 \end{bmatrix} \qquad (2.2)$$

$$Trans(\hat{y}, d) = \begin{bmatrix} 1 & 0 & 0 & 0 \\ 0 & 1 & 0 & d \\ 0 & 0 & 1 & 0 \\ 0 & 0 & 0 & 1 \end{bmatrix}$$

Using the phalange lengths (Table 2.1) and range of motion (RoM) of each

Table 2.3: Volume of workspace

	Volume of workspace (mm^3)	ratio
Human finger	2.60 eˆ5	100%
Robotic finger	1.79 eˆ5	68.7%
Robotic finger with human finger RoM	2.23 eˆ5	85.8%

Table 2.4: Workspace

Volume of workspace (mm^3)	+z (v_+)	-z (v_-)
Human finger (v_{h+}, v_{h-})	2.46 eˆ5	1.43 eˆ4
Robotic finger (v_{r+}, v_{r-})	1.57 eˆ5	2.20 eˆ4
Ratio (robot/human)	63.7%	153.7%

joint (Table 2.2), the workspaces of the human and proposed robotic finger were compared and shown in Table 2.4. The human DIP joint can be driven independently in a limited workspace but has a coupling relationship with the PIP joint during natural flexion/extension motion [34][35]. To simplify the calculation of the workspace, 1:1 coupling relationship between the PIP joint angle and the DIP joint angle of the human and robotic finger, $q_2 = q_3$, was applied. The workspace of a human finger and the robotic finger are illustrated with blue and red colors, respectively. The workspaces of the robotic finger and the human finger show similar shapes but have different sizes due to differences in the length of the phalanges and RoM of joints. The total workspace of the human finger was estimated at 2.60 e^5 mm^3, and the workspace of the robot finger was estimated at 1.79 e^5 mm^3, which was 68.7% of the human finger workspace. The reasons why the robotic finger had a smaller workspace were the short length of phalanges and the small RoM of the MCP AA joint. If the proposed robotic finger has the same RoM as a human finger, it has a workspace of 85.8% of the human finger workspace (Table 2.4).

As shown in the Fig. 2.5(a), the workspace of the finger was divided into the workspace, v_{h+} and v_{r+}, located in the region where $z > 0$, and v_{h-} and v_{r-} located in the region where $z \leq 0$. This is because fingertip positions on the MCP AA axis are singular points where the MCP AA joint cannot generate linear velocity of the fingertip. Although the total workspace of the proposed robot finger is 68.7% of that of the human finger, comparing v_{h-} and v_{r-}, which are workspaces in the $z \leq 0$ region, the workspace of the robot finger is 1.54 times that of a human finger.
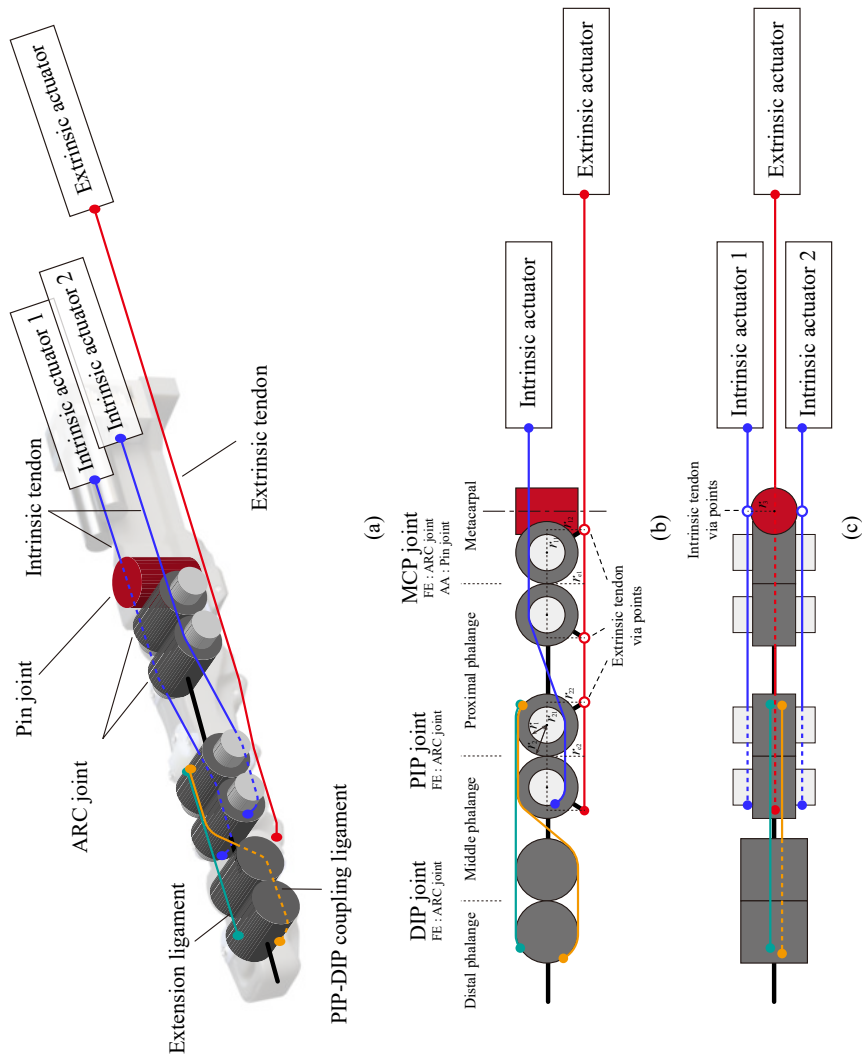
Figure 2.6: The overall structure of the proposed tendon-driven robotic finger. The finger consists of four phalanges and four joints actuated by three twisted string actuators. (a) Isometric view, (b) Lateral view, (c) Top view.

2.2.3 Tendons and Ligaments of the proposed robotic finger

Based on that the velocity of the human fingertip has an uneven velocity distribution during the object grasping process, the tendon path with 5 different tendons and ligaments was proposed (Fig. 2.6). Tendons and ligaments are distinguished according to whether the string is connected to the actuator. The tendon illustrated in the red line is the tendon that transmits the force of the extrinsic actuator, which is located on the outside of the hand, to the joints, and the intrinsic tendons illustrated in blue lines transmit the force of the two intrinsic actuators, which are located on the metacarpal bone, to the joints. As shown in Fig. 2.6(c), the extrinsic tendon passes through the center of the robotic finger. The two intrinsic tendons are located symmetrically, and actuated MCP and PIP FE joints opposite directions, and actuated MCP AA joint. The DIP joint angle has 1:1 coupling relationship with the joint angle of the PIP joint and is actuated passively by the DIP-PIP coupling ligament represented in the orange line.

In order to reduce the complexity of the system, many tendon-driven robotic hands implement extension motion by applying passive components such as springs [13][36][37][38]. Because, unlike the flexion motion, the extension motion and extension forces of the robotic hands has relatively low importance when grasp objects. To reduce the number of actuators, extension motion was implemented using a ligament made of elastic material which was depicted as a green line in Fig. 2.6.

Fig. 2.7 shows the detailed tendon path of the MCP joint and the PIP joint. The extrinsic tendon and intrinsic tendon pass through the MCP joint and the PIP joint, and are fixed in the middle phalanx. The intrinsic tendon maintains

MCP joint

$r_{r1} = 4\ mm$
$r_{m1} = 6\ mm$
$r_{m2} = 12\ mm$

$r_{ma} = 5.5\ mm$

PIP joint

$r_{r1} = 4\ mm$
$r_{r2} = 7\ mm$
$r_{p1} = 4\ mm$
$r_{p2} = 10\ mm$

(a)

(b)
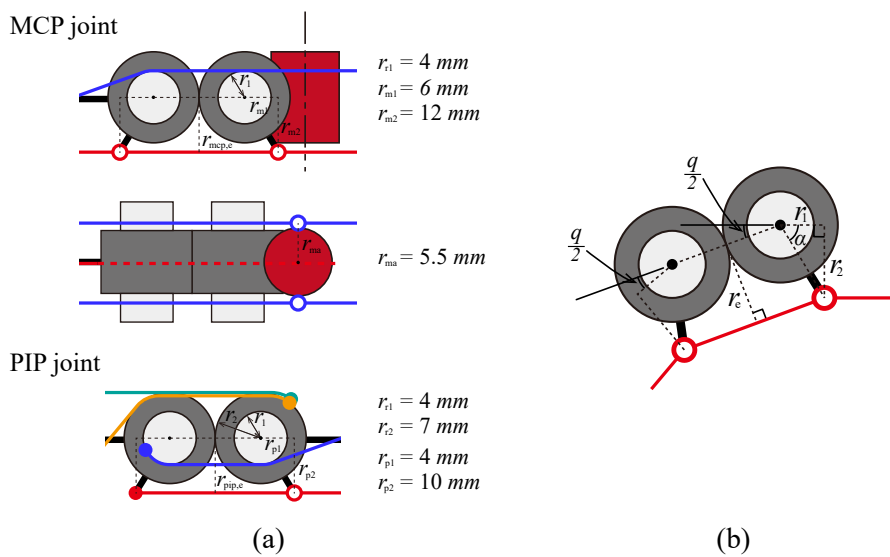
Figure 2.7: Detail structure of metacarpal joint and proximal interphalangeal joint. Metacarpal joint have two degrees of freedom, and proximal interphalangeal joint have one degree of freedom, (a) Tendon routes of metacarpal joint and proximal interphalangeal joint, (b) Variable moments arm of extrinsic tendon

the moment arm for the joint angle of the MCP and PIP flexion/extension joint because it passes over a cylindrical surface of the rolling contact joint as shown in Fig. 2.7(a). However, the extrinsic tendon has a moment arm that increases with joint angles because it passes through fixed points for each phalange (Fig. 2.7(b)) [39]. The moment arms for the MCP and PIP joints of the extrinsic tendon are expressed by joint angle as the equation below.

The joint velocity of flexion/extension joint of MCP, PIP, and DIP are calculated by Equation (2.3) where R is moment arm matrix, and L and $\dot{L}$ are the contraction lengths and velocities of intrinsic and extrinsic tendons which means when the tendons are contracted, $\dot{l}_{ex}$ and $\dot{l}_{in}$ are positive values.

$$
\begin{bmatrix} \dot{q}_1 \\ \dot{q}_2 \\ \dot{q}_3 \end{bmatrix} = \begin{bmatrix} 1 & 0 \\ 0 & 1 \\ 0 & 1 \end{bmatrix} R^{-1} \dot{L}
\tag{2.3}
$$

$$
\begin{aligned}
R =& \begin{bmatrix} r_{mcp,e} & r_{pip,e} \\ -r_{i1} & r_{i2} \end{bmatrix} \\
r_{mcp,e} =& \sqrt{r_{m1}^2 + r_{m2}^2} \cdot \sin(\pi - \arctan(r_{m2}/r_{m1}) - q_1/2) \\
r_{mcp,i} =& \sqrt{r_{p1}^2 + r_{p2}^2} \cdot \sin(\pi - \arctan(r_{p2}/r_{p1}) - q_2/2) \\
\dot{L} =& [\dot{l}_{ex} \quad \dot{l}_{in}]^T
\end{aligned}
\tag{2.4}
$$

2.2.4 Decoupled fingertip motion in the sagittal plane

Due to the difference in moment arms of intrinsic and extrinsic tendons, each tendon generates a different motion of the finger. Fig. 2.8 shows the tendon path of the robot finger in the sagittal plane and the movement of the fingertip when
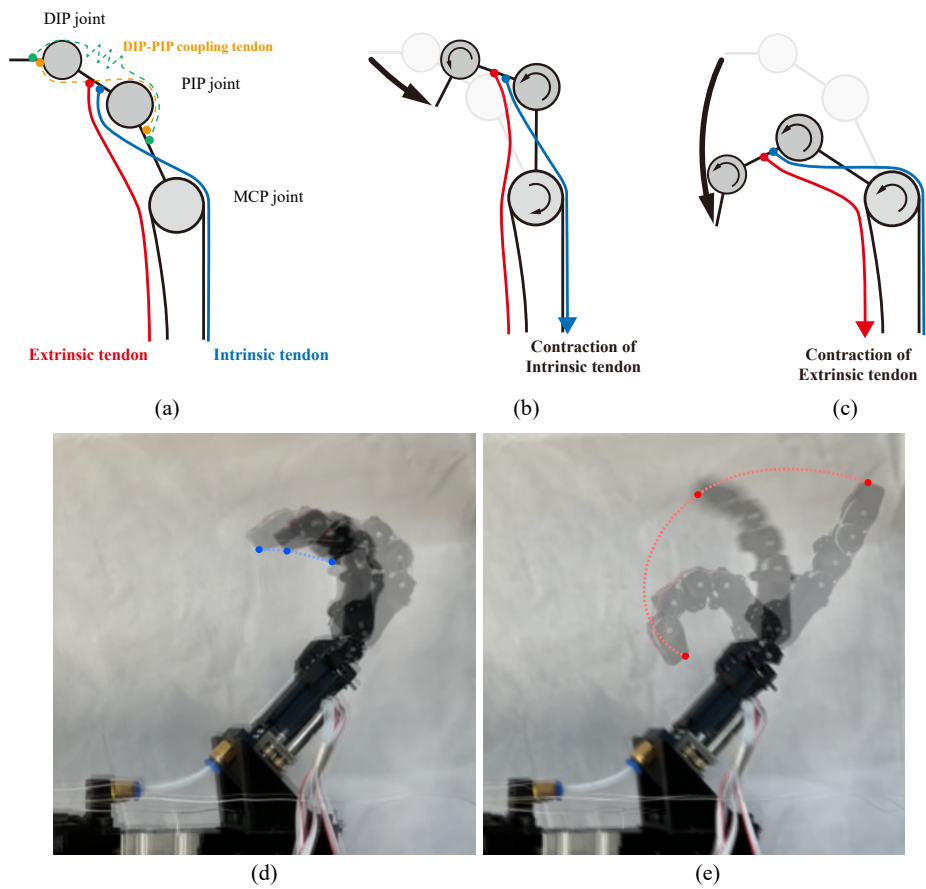
Figure 2.8: The differences between fingertip motions generated by intrinsic and extrinsic tendons. (a) Tendon route of proposed robotic finger, (b) Finger motion with contaction of intrinsic tendon, (c) Finger motion with contraction of extrinsic tendon.

each tendon is actuated. Similar to the FDS and FDP of human hand muscles, the extrinsic tendon has a moment arm in the same direction at the MCP and PIP FE joints and is responsible for bending the entire finger as shown in Fig. 2.8 (c). In contrast, the intrinsic tendon has a moment arm in the opposite direction to the MCP and PIP flexion/extension joints, and is responsible for actuating the fingertip toward the center of the MCP joint (Fig. 2.8(b)). And, Fig. 2.8(d) and (e) show the motion of a manufactured robotic finger when actuated by only one of the intrinsic and extrinsic actuators. Using the proposed tendon path, the fingertip motion by each actuator can be decomposed as similar to the motion generated by human muscles.

Fig. 2.9 shows the posture of the robotic finger and the velocity ellipsoid at the tip. Unlike general actuators which are capable of bidirectional actuation, linear actuators using tendons can only generate contraction force, and the tendon-driven robotic finger can implement only a part of the velocity ellipsoid. The velocity ellipsoid represented by the blue dotted lines at the tip in each posture is a velocity ellipsoid that can be generated by bidirectional actuators, and the parts represented by the red solid lines are a velocity ellipsoid that can be generated when using a linear actuator that can only generate contraction force. The fingertip velocity in the sagittal plane was calculated using the Equation (2.5) to observe the change of the velocity ellipsoid according to the ratio of the maximum contraction velocity of the actuators connected to different tendons.

$$V_{tip} = J \cdot \begin{bmatrix} 1 & 0 \\ 0 & 1 \\ 0 & 1 \end{bmatrix} \cdot R^{-1} \cdot \dot{L} \qquad (2.5)$$
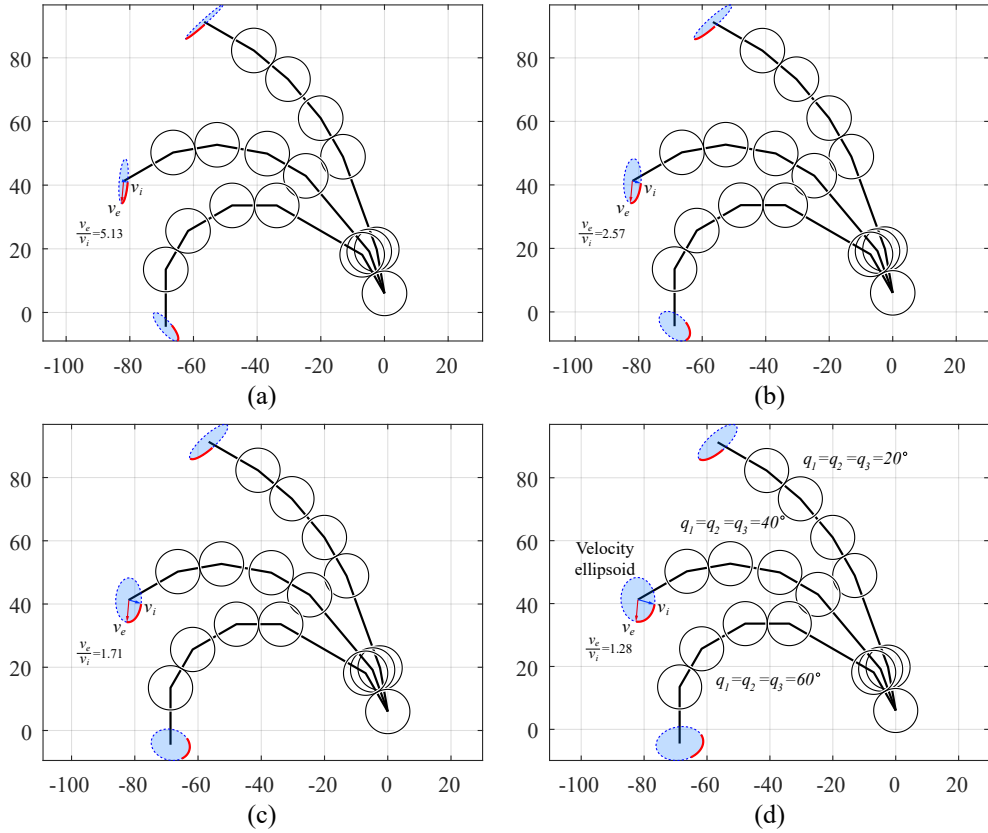
Figure 2.9: Velocity ellipsoids of the robotic finger in sagittal plane with different maximum contraction velocity ratio between intrinsic and extrinsic actuators. (a) $v_e : v_i = 4 : 1$, (b) $v_e : v_i = 2 : 1$, (c) $v_e : v_i = 4 : 3$, (d) $v_e : v_i = 1 : 1$

$$\dot{L} = V_{max} \cdot A$$

$$V_{max} = \begin{bmatrix} v_{ex,max} & 0 \\ 0 & v_{in,max} \end{bmatrix}$$

(2.6)

$$A = [a_{in} \quad a_{ex}]^T$$

In Equation (2.5), V_{tip} represents the fingertip velocity in sagittal plane ($q_0 = 0$ and $\dot{q}_0 = 0$), and J is the jacobian matrix from $\{0\}$ to $\{tip\}$. To observe the effect of the variation in the maximum contraction velocity of each actuator, the contraction velocity, $\dot{L}$, was expressed as $V_{max} \cdot A$ where V_{max} represents the maximum contraction speed of each actuator and A is the activation matrix where each component represent the activation of each actuator value between from 0 to 1 (Equation (2.6)).

Fig. 2.9 shows the velocity ellipsoid, V_{tip} when $|A| = 1$, of the robotic finger in the sagittal plane. The shape of the velocity ellipsoid changes as the ratio of the maximal contraction velocity between the intrinsic and extrinsic actuators changes. Fig. 2.9 (a)(b)(c) and (d) show velocity ellipsoid variation when the maximum contraction velocity ratio varied from 1:4 to 1:1 with three different joint angles. The maximum contraction velocity of the extrinsic actuator was fixed at 1, and then the maximum contraction speed of the intrinsic actuator was slowed down. V_{in} illustrated by the blue arrow represents the velocity when only the intrinsic actuator only was activated, and V_{ex} illustrated by the red arrow represents the velocity generated when the extrinsic actuator is activated alone. As the maximal contraction speed of the intrinsic actuator increases, it can be confirmed that the velocity ellipsoid becomes closer to a circular shape. In Chapter 2.1, the speed ratio of the human fingertip during grasp

was averagely 2.48. When the maximum contraction velocity of the intrinsic actuator was half of that of the extrinsic actuator, the fingertip velocity ratio of the proposed robotic finger was 2.57 which is similar to that of a human finger (Fig. 2.9(b)).

Various robotic hands have been developed, until now, using the same actuators for all joints regardless of the motions and tasks to be implemented. Using multiple numbers of identical actuators reduces the design complexity and has the advantage in terms of maintenance. However, there is a problem that size and weight cannot be optimized, and as a result, robotic hands with a high degree of freedom become heavier than human hands. To improve the size and weight of the robotic hand, the intrinsic tendons, which require relatively slow contraction velocity, were connected to a small-sized actuator. And the actuators were located inside the hand. Due to the small size of the actuator, it was possible to place two actuators inside the metacarpal while maintaining the small size and light weight of the robotic finger.

One of the advantages of robotic hands with separated intrinsic/extrinsic tendon paths is that adaptive grasping can be implemented using only a relatively fast extrinsic actuator. Adaptive grasping is a mechanism used to compensate for the low degree of freedom of under-actuated robotic hands and increases the success rate of object grasping by adjusting the joint angle to fit the shape of a target object. When only the extrinsic actuator is actuated without contact on the phalanges of the finger, the MCP, PIP and DIP joint angles have a certain coupling relationship due to the intrinsic tendon and PIP-DIP coupling tendon. However, when contact occurs between the proximal phalange and the object, the joint angle of the MCP FE joint is fixed by the contact

force, but the PIP joint and the DIP joint continuously flex. As a result, the finger posture adapts to the shape of the object only by actuating the extrinsic actuator. In the process of adaptive grasping, slack occurs in the intrinsic tendon.

Chapter 3

ELASTOMERIC CONTINUOUSLY VARIABLE TRANSMISSION COMBINED WITH TWISTED STRING ACTUATOR

3.1 BACKGROUND & RELATED WORKS

The mimicking of human hand motion constitutes a vital research direction demanded by many modern robotic applications, which include humanoid robots that imitate human motion, prosthesis to replace human hands, and wearable devices that assist human hand movements. Until now, several devices have been developed using electric motors, and robotic hands that employ new types of actuators, like pneumatic actuators and shape memory alloy actuators, have been designed [40][41][42]. Various approaches, concerning robotic hands, have been investigated for improvement in terms of dexterity, force, weight, and volume [43][44].

However, to our knowledge, there exists no robotic hand that simultaneously realizes the weight, size, force, and dexterity of the human hand and continues to remain a challenge [44]. One of the several reasons why contemporary robotic hands cannot surpass the traits of human hands is the challenge associated with reducing the size of the actuators without losing power capacity [45]. Therefore, the properties of muscles, efficient muscle placement using tendon and adaptable reduction ratios are required for a versatile end-effector with high degrees of freedom in small proportions like human hands [46][47][48].

The use of electric motors with a variety of mechanisms that convert the rotational force of a motor into linear forces is a commonly used method to achieve the characteristics of muscles. By converting rotational forces into linear forces and using strings as tendons, heavy and bulky actuators can be placed on the forearm. Schmitz et al. [22] placed tendon-driven actuators in the palm and forearm to maintain versatility in small robotic hands. Furthermore, Bridgwater et al. [23] designed a robotic hand using a tendon connected to an electric motor with a ball screw.

Twisted string actuator (TSA) is a method comprising electric motors and strings and is an actuator that employs the contraction force that occurs when multiple strings are twisted [49][50]. As the TSA converts rotational the force of a motor to linear force using a lightweight and straightforward structure, it has been applied to various robotic systems. Palli et al. [12] implemented a robotic hand and wrist with 22 degrees of freedom, using 24 TSAs in the forearm. However, a TSA with a high reduction ratio is not appropriate to be accelerated to the contraction velocities of muscles. To overcome the limitation of TSAs, TSAs with variable reduction ratio mechanisms have been studied by
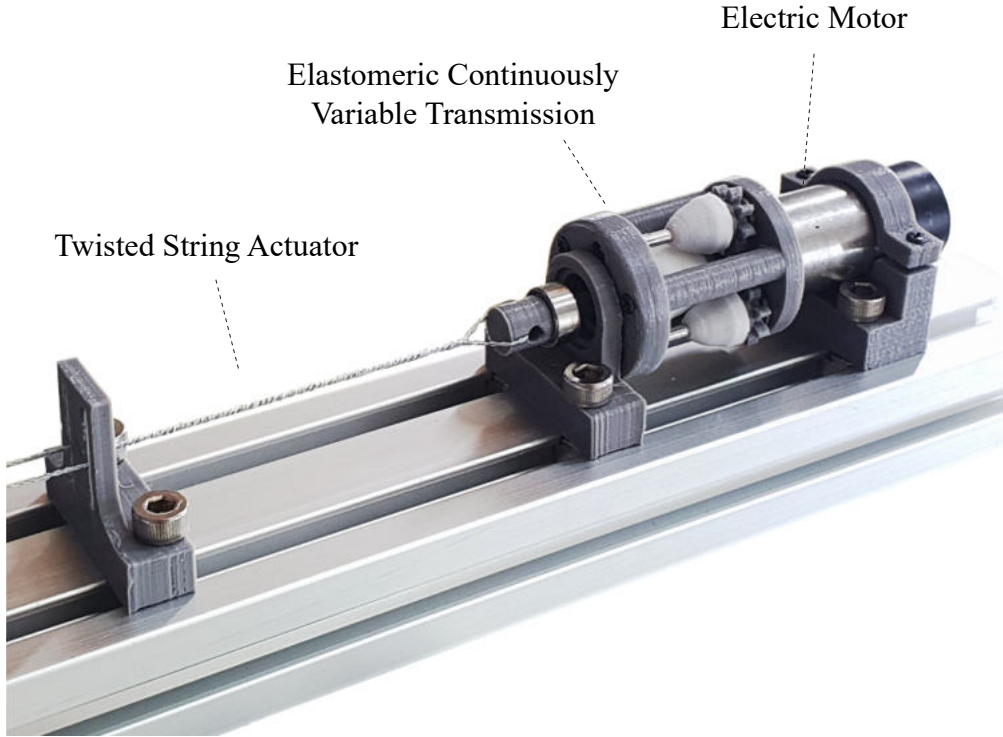
Figure 3.1: ElaCVT-TSA: Combination of ElaCVT and TSA

adjusting the reduction ratio by means of an external load, which is one of the properties of muscles.

Jeong and Kim [51] designed a 2-speed small transmission mechanism based on the TSA mechanism consisting of two motors. One motor provides the contraction force, while the other one is used to switch between the force mode and speed mode, by changing the twisted radius. Furthermore, they demonstrated the feasibility of a 2-speed dual-mode TSA by applying it to a robotic hand. However, the mode change process interrupted continuous motion. Singh et al. [52] proposed a passively adjustable TSA with springs placed between two strings that could maintain a small reduction ratio under a small external force. This passive adjustable TSA showed that continuous variable transmis-

sion (CVT) could be effectively used to cover the operating region of muscles. However, it still remains as a limitation that the amount of reduction ratio variation decreases as the TSA contracts, because the change of reduction ratio depends on the amount of spring compression.

Various types of CVTs have been developed, and many commercial products already exist. However, these CVTs have a complex structure in order to transmit high torque without slip. Moreover, when changing the reduction ratio, these CVTs employ use hydraulic pumps to overcome reaction forces like friction. Although CVTs, which convert the reduction ratio passively, are used in relatively low power engines such as motorcycles, these CVTs use inertia forces, which are generated at high rotational speeds. Therefore, it is impossible to reduce the size and weight of existing CVTs for robotic applications.

To expand the operating region of TSAs and mimic the force-velocity curve (FV curve) of muscles, in this study, we designed a novel elastomeric CVT (ElaCVT), which can be applied to small-size robotic applications such as robotic hands (Fig. 3.1). The reduction ratio of the ElaCVT is passively changed by means of an external load on the TSA that compresses the elastomer. Additionally, by combining the ElaCVT and TSA (ElaCVT-TSA), we propose a new concept for the linear actuator module, which can be used as a muscle-like actuator. The twisted string mechanism amplifies the relatively small reduction ratio of the ElaCVT.

In Section 3.2, we compare the FV curves of muscles and electric motors and demonstrate the necessity of a CVT to mimic the force-velocity characteristics of muscles. In Section 3.3, the structure of the proposed ElaCVT-TSA is described and the passively changing reduction ratio mechanism by means of an
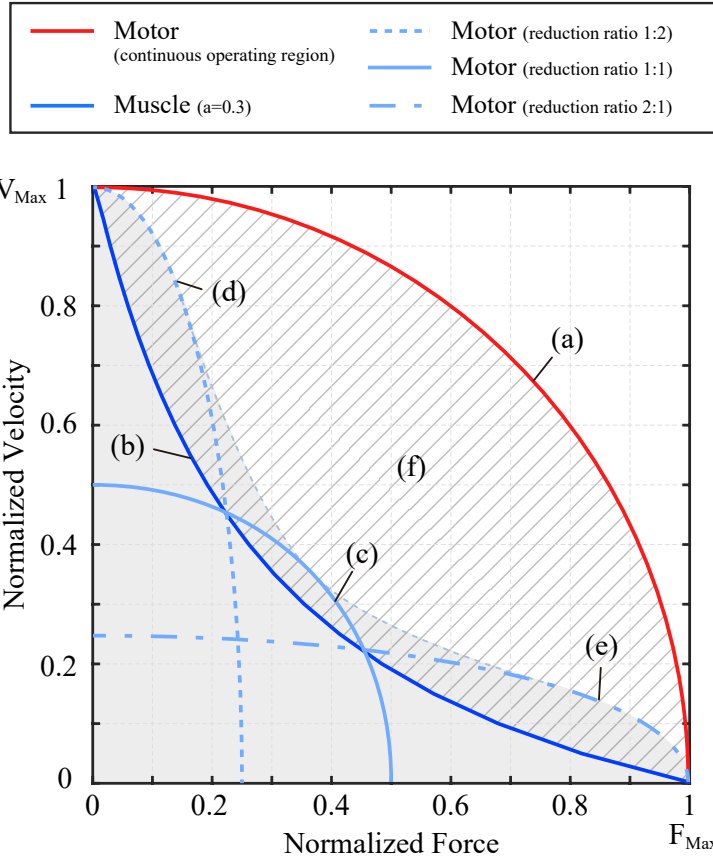
Figure 3.2: (a) FV curve of an electric motor, (b) FV curve of muscle (a=0.3), (c), (d), (e) FV curves of an electric motor with CVT, (f) unused area when simulating muscle motion. The power capacity of (a) is four times that of (c).

external force is explained. To demonstrate the performance of the ElaCVT-TSA, the experimental results of the contraction test, with various external loads, are shown in Section 3.4.

Table 3.1: Comparison between two commercially available electric motors with different power capacities

Product Name	Maxon,EC-max 16	Maxon,EC-max 22
Power capacity	5 W	12 W
Nominal speed	5840 rpm	8040 rpm
Nominal torque	3.23 mNm	10.2 mNm
Diameter	16 mm	22 mm
Length	24 mm	32 mm
Weight	36 g	83 g

3.2 COMPARISON OF OPERATING REGIONS

Various actuators have different operating characteristics. Comparing the operating region, using the *FV curve* of different actuators, is an essential step in selecting appropriate actuators.

The continuous operating region of a general electric motor can be represented as a quadrant of the circle owing to the physical limitations of the materials used in motors, such as insulation damage of the wire that can be caused by high temperature. The mechanism that converts torque of the motor into linear force can be regarded as a reducer with a fixed reduction ratio; the FV curve of the linear actuator, using an electric motor, can be represented by the same quadrant as the operating region of the motor. The red line in Fig. 3.2(a) is the normalized FV curve of a linear actuator.

The FV curve of muscles can be approximated using the following hyperbolic equation [53].

$$(P + a)(v + b) = (P_0 + a)b = const. \tag{3.1}$$

The variables P, P_0, and v are the load, maximum isometric force, and contraction velocity of the muscle, respectively. The terms a and b are constant parameters obtained experimentally for each muscle. For mammalian skeletal muscles, a/P_0 approximately lies between 0.15 to 0.30 [54]. The normalized FV curve for muscles, whose maximum isometric force (P_0) and maximum contraction velocity are 1, with $a = 0.3$, is depicted in Fig. 3.2(b).

The operating regions of the muscle and electric motor have different shapes. The muscle has a concave shape, and the electric motor has a convex shape. The hatched area (Fig. 3.2(f)) between these two curves is unusable when mimicking the motion of muscles, but it occupies a large portion of the operating region of the motor. The muscle with the smaller parameter a result in an FV curve that has a more concave shape, and larger hatched area. However, the use of a motor with smaller power capacity cannot achieve the maximum speed or force of the muscle, and it is, therefore, impossible to reduce this area without the use of additional mechanisms.

Fig. 3.2(c), (d), and (e) show the FV curves of the motor with a CVT, whose change in reduction ratio is 2:1, 1:1, and 1:2. The grey area below these graphs represents the operating region of the motor with the CVT, and effectively covers the operating region of the muscles. In this case, the required power capacity of the motor with CVT is four times smaller than the power capacity of the motor without CVT. In Table 3.1, a compression of the specifications of two commercially available motors with different power capacities is shown. The first is EC-max 16, 5 W motor, which is used in this study. The second one is EC-max 22, which has a 12 W power capacity. The EC-max 16 weighs less than half the EC-max 22, and this shows that there is a significant weight

difference, depending on the power capacity of the motors. In robotic hands that employ multiple actuators, if the ElaCVT-TSA is designed lighter than an actuator with a large unused region, the weight of the entire system can be significantly reduced.

3.3 DESIGN OF THE ELASTOMERIC CONTINUOUS VARIABLE TRANSMISSION

In this section, the actuator module that combines the ElaCVT and TSA is introduced. Furthermore, the structure and mechanism of the newly proposed ElaCVT, including the advantages of the ElaCVT are explained.

3.3.1 Structure of ElaCVT

In Fig. 3.3(a), an ElaCVT-TSA is depicted, and the inner structure of the ElaCVT is illustrated in Fig. 3.3(b). The ElaCVT consists of a rigid lateral disc and elastomer, which is directly connected to the output shaft. The input torque from the motor is transmitted to the lateral disc by means of spur gears to the output shaft using friction between the lateral disc and elastomer. The mechanisms that convert the rotational force to linear force can be applied to the end of the ElaCVT. The ball screw and lead screw are commonly used mechanisms. However, in this study, we employ the TSA. Although the mechanisms using screws have better efficiency and are more reliable than the TSA, they are not only heavier than the TSA but also require an additional mechanism to enable axial movement. On the other hand, the ability to self-compressed and flexible features fo the TSAs facilitate axial movement without the need

for additional mechanisms, which reduces the weight of the overall system. The output shaft of the ElaCVT is connected to the TSA, and the torque is converted into a linear force. With this structure, the external load applied to the end of the TSA can directly compress the elastomer the along axial direction, and change the reduction ratio continuously (Fig. 3.3(b)).

Since the maximum static friction between the elastomer and each lateral disc is equal, the higher the number of lateral discs used, the larger the torque that can be transmitted without slip. In this study, three lateral discs were used, considering the size of elements such as bearings. All the parts were manufactured using a 3D printer, except the bearings and rotating shafts. The ElaCVT has a cylindrical shape with a length of 27 mm, a diameter of 24 mm (Fig. 3.3(a)), and weighs 12 g.

3.3.2 Design of Elastomer and Lateral Disc

The elastomer is a crucial part that allows the change of the reduction ratio, and the material and shape of the elastomer directly affect the performance of the ElaCVT. Various shapes of elastomer were tested, using silicone of multiple stiffnesses. The stiffness of the elastomer should be selected considering the output torque of the motor. If a low torque motor with a high stiffness elastomer is used, the motor reaches the torque limit before the reduction ratio changes. Conversely, if a high torque motor with a low stiffness elastomer is used, a large part of the operating region of the motor is used, only at a high reduction ratio. A silicone with 12 Shore A was used, and the lateral discs were covered with a thin layer of the same silicone to prevent wear of the lateral discs and elastomer.

The elastomer was shaped into a cone to increase the change in the reduction
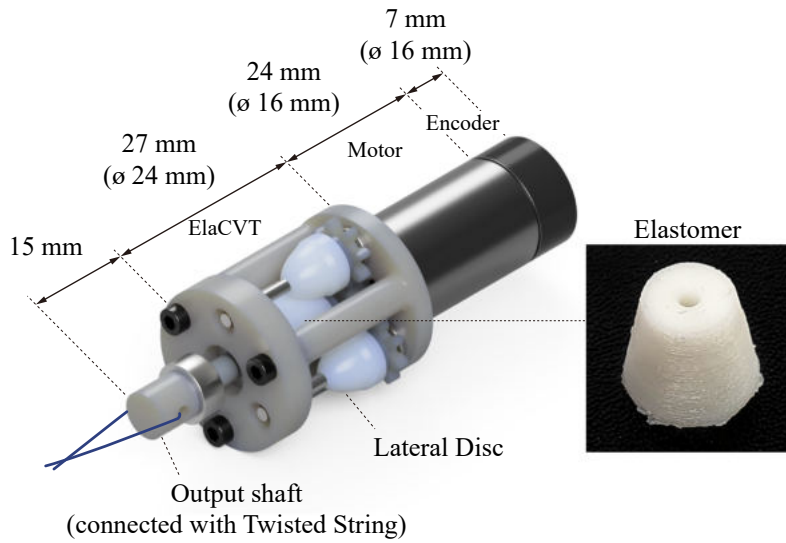
(a)
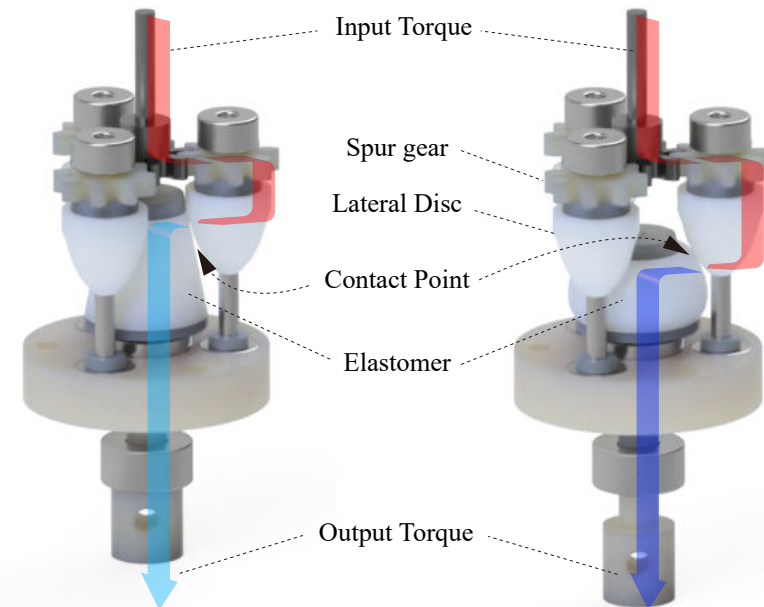
(b)

Figure 3.3: Configuration of the ElaCVT-TSA, (a) Dimension of the ElaCVT-TSA, (b) Inner structure of the ElaCVT without the outer case. The left image depicts the maximum velocity mode, while the right image depicts the maximum torque mode.
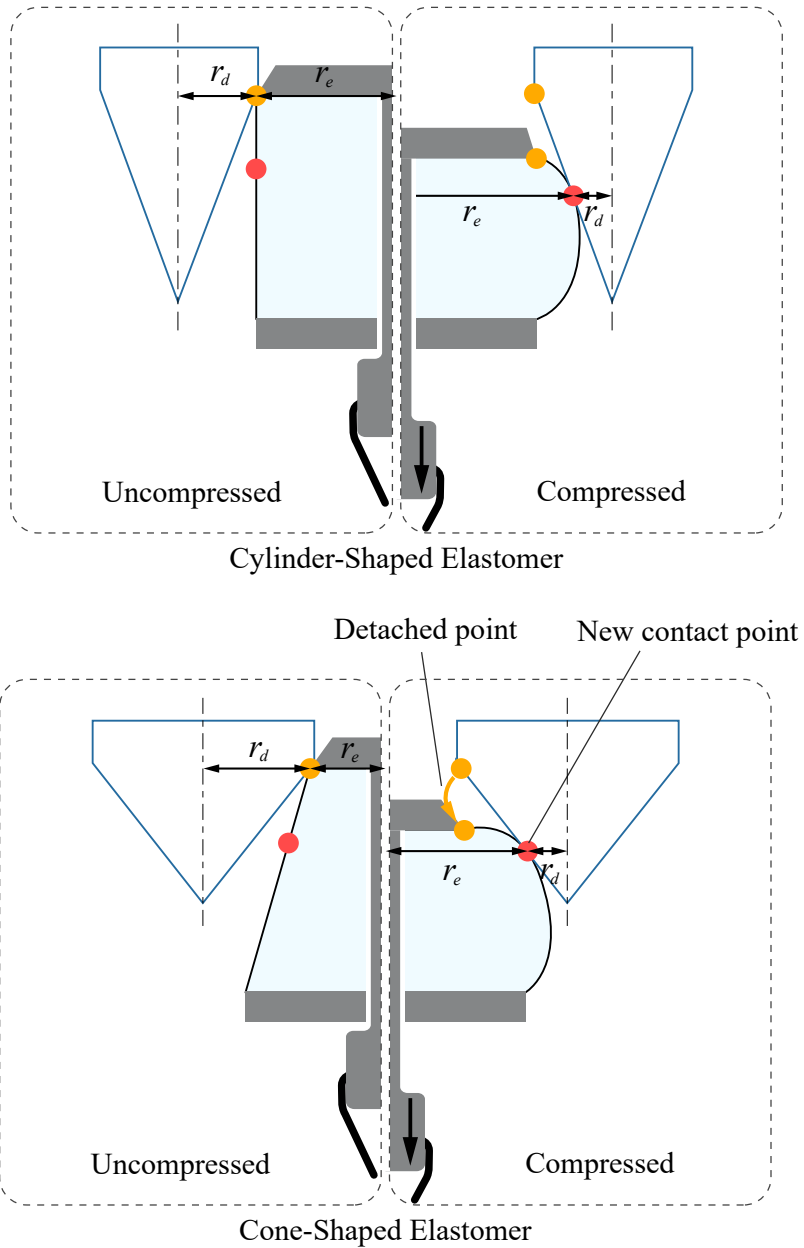
Figure 3.4: Different lateral disc shapes depending on the shapes of the elastomer. The orange points are the contact points when the elastomer is uncompressed, and red points are newly attached contact points after compression. Using a cone-shaped elastomer, the amount of contact radius change increases.
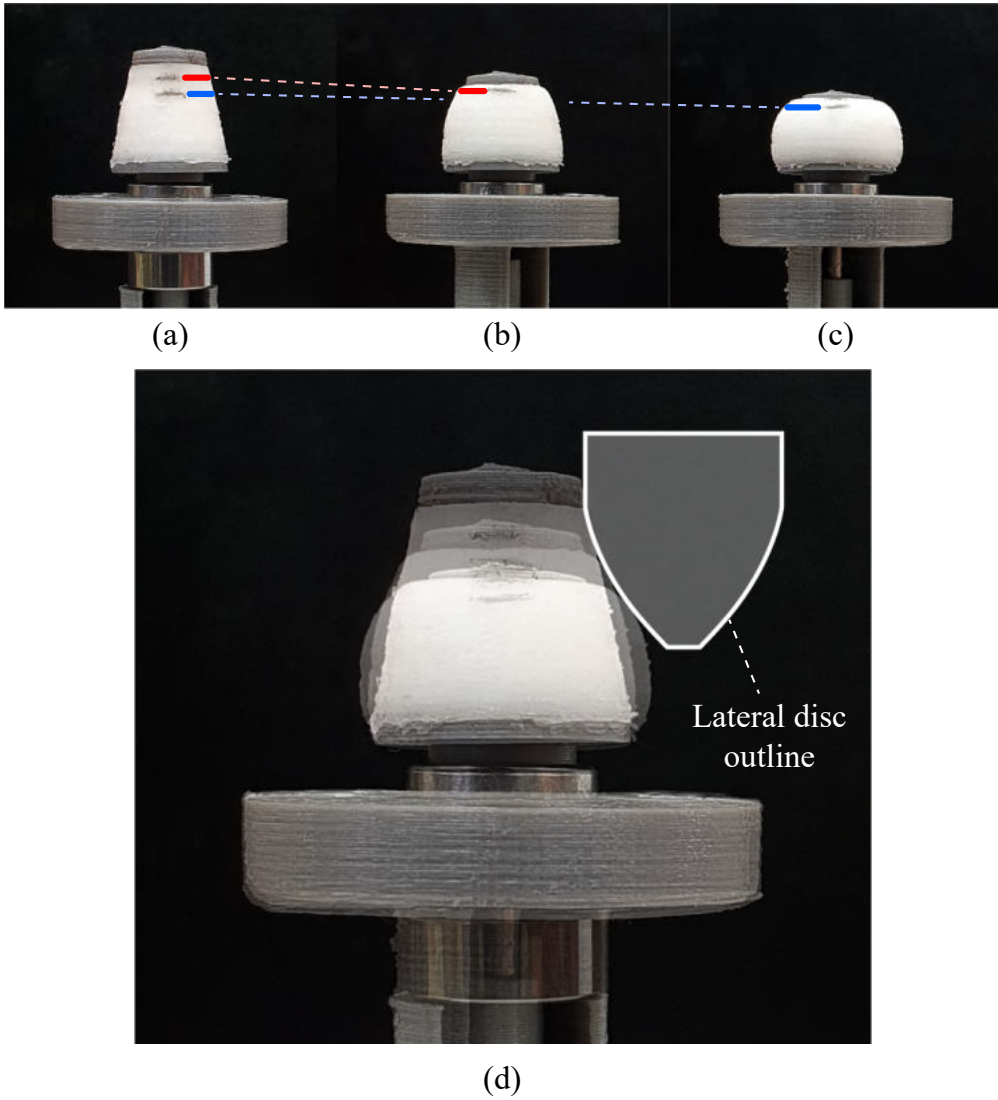
Figure 3.5: Deformation of elastomer according to the amount of compression, (a) 0 mm, (b) 2 mm, (c) 4 mm, red and blue line indicates the same location on the elastomer, respectively. (d) Overlapped images with the outline of the lateral disc.

ratio. Simplified shapes of the lateral discs, depending on the cylinder-shaped and cone-shaped elastomers are illustrated in Fig. 3.4. When the elastomer is compressed, it forms new contact points by filling the gaps between the lateral discs and the elastomer. In Fig. 3.4, r_e and r_d are the radii from the rotational axis of the elastomer and the lateral disc to the contact point. The ratio of these radii, $r_e : r_d$, represents the reduction ratio of the ElaCVT. As the elastomer is compressed, r_e becomes larger, and r_d decreases, the transmitted torque is amplified, and the angular velocity decreases. The use of a cone-shaped elastomer can increase the radial change of the lateral disc and elastomer disc. Therefore, a larger reduction ratio change is implemented.

Elastomers applied to the ElaCVT have a lower diameter of 12 mm, an upper diameter of 8 mm, and a height of 10 mm with a weight of 1 g. The size of the elastomer was selected, considering the size and output of the motor used (Maxon, EC-max 16). To determine the outer line of the lateral disc corresponding to the elastomer, we conducted deformation experiments. Deformed elastomers and the outline of the lateral disc are depicted in Fig. 3.5. We then interpolated the outermost points to complete the outline of the lateral discs. To prevent the disconnection between the elastomer and lateral discs, due to manufacturing errors, we employed a 5% enlarged outline to produce the lateral disc.

The size of the ElaCVT can be reduced by using a small elastomer. However, given that transmittable torque is also reduced when using a smaller elastomer, the appropriate size of the elastomer should be considered.

3.3.3 Advantages of ElaCVT

The ElaCVT, which implements the reduction ratio change by using the shape deformation of the elastic body, has advantages that are suitable for the robotics field.

First, in the reduction ratio change process, the previous contact point detaches and does not slip to move to the new contact point, and a new contact point is generated through the deformation of the elastic body. This process reduces friction resistance. The differently located contact points as the elastomer is compressed are shown in Fig. 3.5.

Second, due to the above advantage, the structure of the ElaCVT can be simplified, given that the load on the output shaft is sufficient to compress the elastomer, unlike conventional CVTs that require a linear actuator.

Third, when combined with a reducer that converts rotational force to linear force, the reduction ratio is changed passively by the linear force, applied to the end, without any additional mechanism. Thus, the combination of TSA and ElaCVT facilitates the actuator module, which simulates muscle characteristics, through the light and straightforward structure.

Additionally, due to the internal structure of the ElaCVT, the motor shaft is decoupled from the output shaft along the axial direction. Any additional structures, such as thrust bearings, are not required to prevent damage to the motor against high axial loads or impacts at the output shaft.
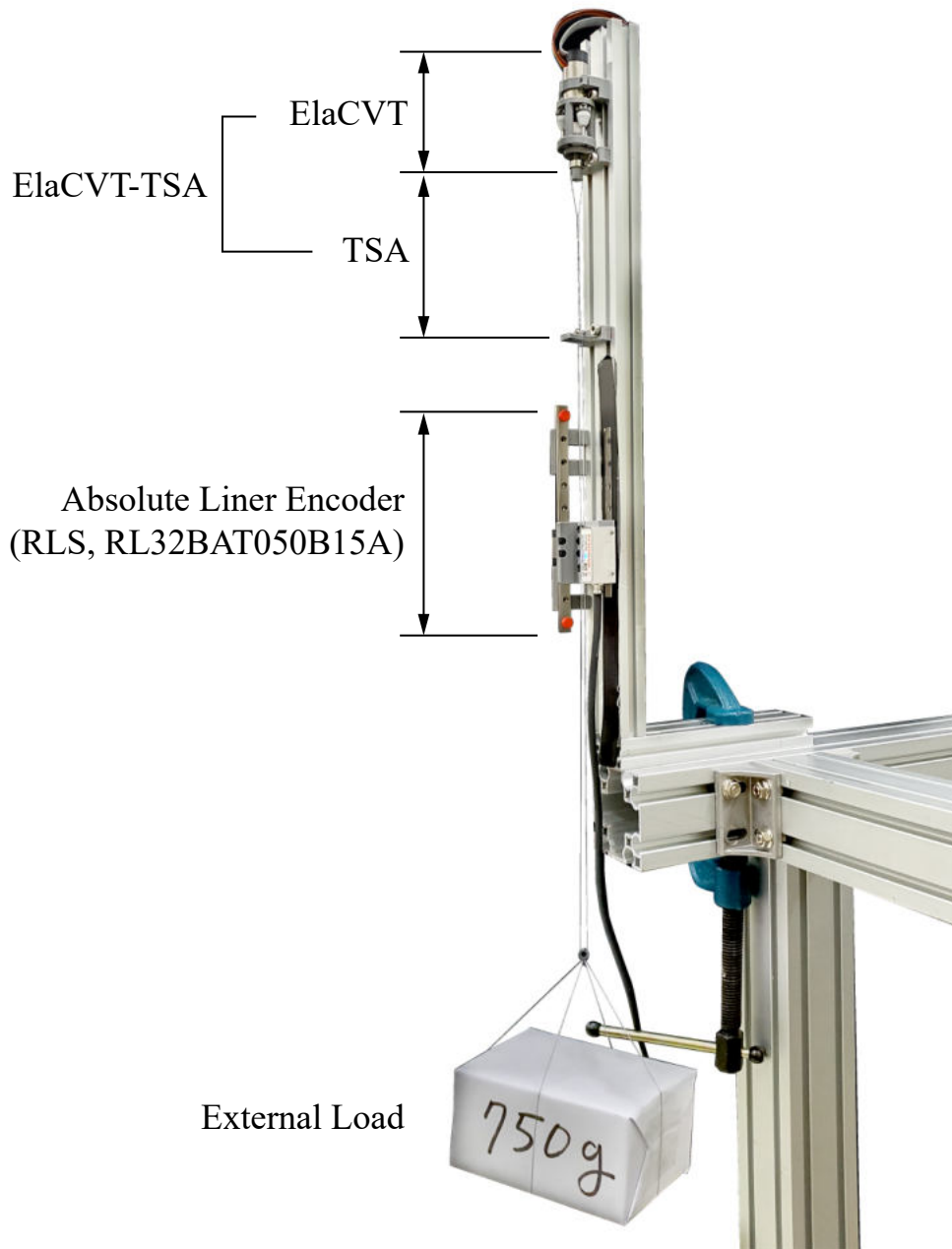
Figure 3.6: Experimental setup to evaluate ElaCVT-TSA

3.4 PERFORMANCE EVALUATION

To evaluate the performance of the newly proposed ElaCVT-TSA, an experimental setup was designed. In this chapter, the experimental setup was introduced, and the reduction ratio change capability of the ElaCVT was evaluated through the contractions under different external loads.

3.4.1 Experimental Setup

In Fig. 3.6, the experimental setup used to evaluate the performance of the ElaCVT-TSA is illustrated. The string used for the TSA was the Dyneema fishing line, whose diameter was 0.5 mm. Without external load, the distance from the string hole on output shaft to string slit was 10 cm. At the end of the TSA, an absolute linear encoder (RLS, RL32BAT050B15A) was installed to measure the contraction length. To reduce the influence of string elongation on the experimental results, the contraction with an external load of 1.75 kg was repeated 50 times before the experiments.

3.4.2 Contraction with Fixed external load

To evaluate the primary purpose of the proposed ElaCVT-TSA, simulating a muscle-like FV curve, the contraction length was measured under different external loads, which ranged from 0.25 kg to 1.75 kg. In all experiments, the motor was controlled at a constant speed. Fig. 3.7 shows the results of the contraction length from 0 cm (untwisted) to 4.8 cm, maintaining a motor speed of 2000 rpm. As the external force increased, the time taken to reach the target point increased, which implies that the external force deformed the elastomer of
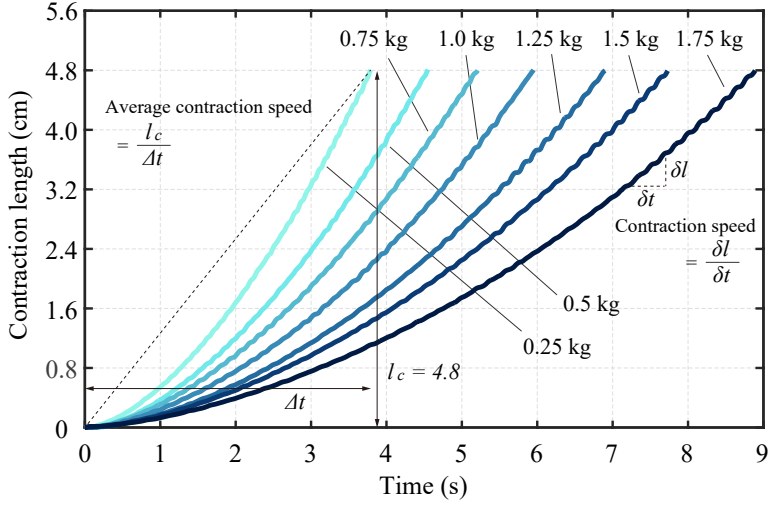
Figure 3.7: Contraction length with different external loads under constant motor speed, 2000 rpm. With constant motor speed, the contraction speed decreases as contraction length increases due to TSA. Average contraction speed was used to exclude the effect of TSA when evaluated the reduction ratio change of ElaCVT.
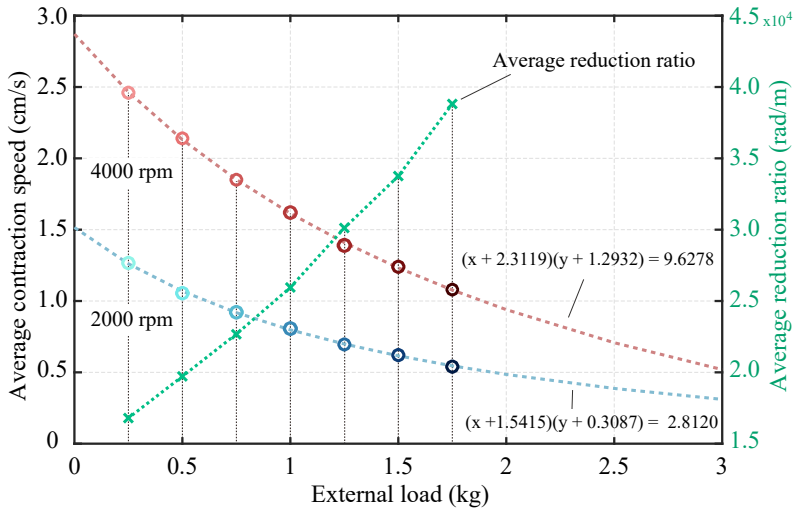
Figure 3.8: FV curves of the ElaCVT-TSA under different motor speeds, 2000 rpm, and 4000 rpm. Circle points represent experimental data. The green dash line shows the average reduction ratio of the ElaCVT-TSA under different external loads.

the ElaCVT. Moreover, the reduction ratio was converted to a high reduction ratio. However, the results show that the contraction speed of the ElaCVT-TSA with a constant motor speed increased as the contraction length increased, because the reduction ratio of the TSA decreased. To exclude the effect of the TSA on the reduction ratio, the average contraction speed was used to construct the FV curves and to calculate the average reduction ratio in Fig. 3.8.

The FV curves of the ElaCVT-TSA are shown in Fig. 3.8. The same experiments were repeated using a motor speed of 4000 rpm, and the results are shown together. As the motor speed doubled, the average contraction speed doubled in all cases, which implies that the ElaCVT is only affected by the magnitude of the external force, and not the speed and torque of the motor. The experimental data are fitted with a hyperbolic function, which represents the FV curve of muscles, and the functions are plotted as dotted lines in Fig. 3.8. Each calculated hyperbolic function shows that the experimental results simulated the FV curve of the muscle.

The green dash line in Fig. 3.8 shows the average reduction ratio which was changed under the different external loads. The average reduction ratio at 1.75 kg was averagely 2.31 times the average reduction ratio at 0.25 kg (from 16776 rad/m to 38811 rad/m).

The input torque of the TSA is proportional to the output force at the same contraction length [49]. Fig. 3.9 shows the motor torque according to the contraction length under 0.5 kg, 1.0 kg, and 1.5 kg external loads, and the experiments were conducted at a motor speed of 2000 rpm. By subtracting the no-load torque, the average motor torques required for the contractions for each experiment are found to be 0.46 mNm, 0.74 mNm, and 1.02 mNm.
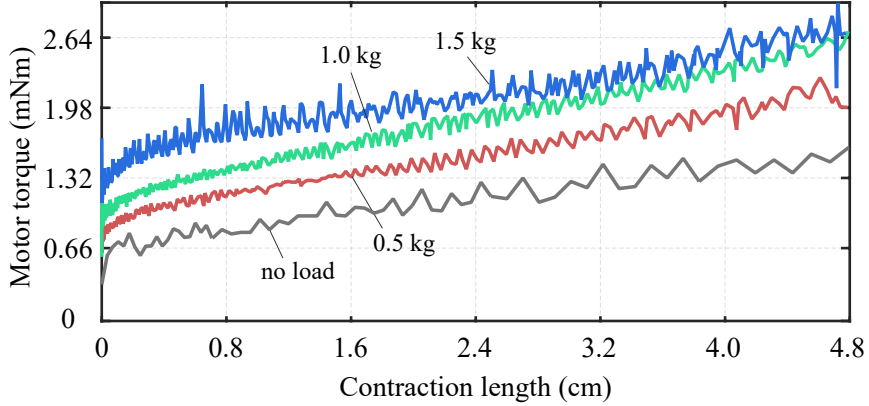
Figure 3.9: Motor torque with the different external loads, 0.5 kg , 1.0 kg, and 1.5 kg. The motor torque increased because the reduction ratio of TSA decreases as TSA contracts.

Using the average motor torques, the efficiency of ElaCVT can be calculated as $\eta = P_{out}/P_{in}$ where P_{in} is input power, which is the production of motor torque and angular velocity, and P_{out}, which is the production of external load and average contraction speed. The efficiencies under 0.5 kg, 1.0 kg, and 1.5 kg external loads at 2000 rpm are 56%, 52% and 44%, respectively.

The reduction ratio at 1.5 kg increased to 1.70 times the reduction ratio at 0.5 kg (from 19853 rad/m to 33727 rad/m). The motor torque should have increased 1.76 times with the tripled external load, given that the 1.70 times increased reduction ratio. However, the average motor torque of the ElaCVT-TSA increased to about 2.22 times (from 0.46 mNm to 1.02 mNm). This difference was partly attributed to the friction between the elastomer and lateral discs. Ideally, the contact points between the elastomer and the lateral discs should be point contacts. However, the lateral discs were scaled up to ensure sufficient friction. This created an area where slip occurred, resulting frictional losses.
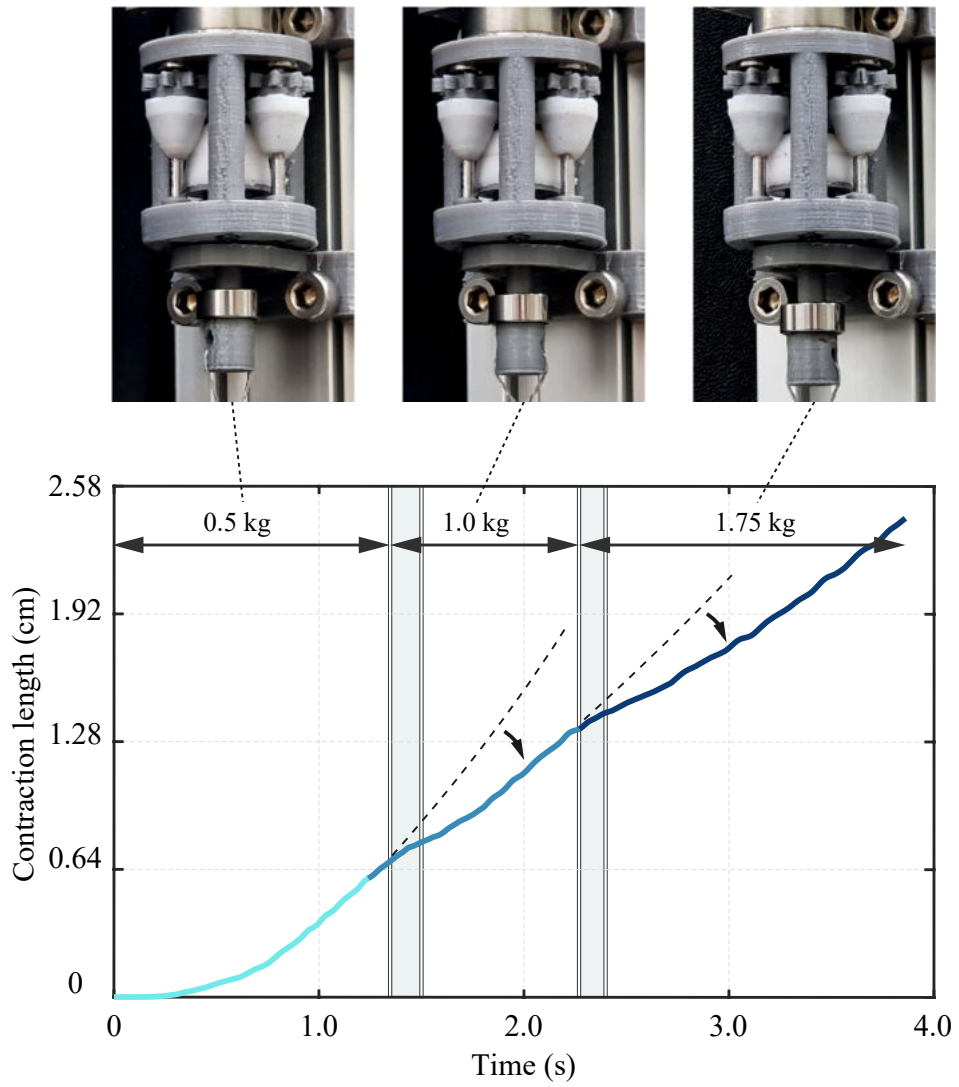
Figure 3.10: Contraction length with gradually increased external load

3.4.3 Contraction with Variable external load

The advantage of the ElaCVT-TSA is that the reduction ratio is passively adjusted depending on the external load regardless of the operation of the motor. This does not generate any discontinuities in the process while changing the reduction ratio. To evaluate this property, an experiment was conducted where the external load increased gradually as the ElaCVT-TSA contracted. The motor was controlled at a constant speed of 2000 rpm.

In Fig. 3.10, the contraction length of the ElaCVT-TSA over time and shape of the elastomer at each external load are shown. The reduction ratio of the ElaCVT changed smoothly as the load increased to 0.5 kg, 1.0 kg, and 1.75 kg. Moreover, that the elastomer was compressed gradually was observed. The result consists of multiple pieces of the results of the fixed external load shown in the previous section. As shown in Fig. 3.7, the contraction speed increased as the TSA contracted under the constant motor speed. However, the contraction speed decreased in grey regions, shown in Fig. 3.10, because the reduction ratio increased by means of the passively deformed elastomer.

3.4.4 Performance variation of ElaCVT over long term usage

The power from the input shaft is transmitted to the output shaft by the contact force between the lateral disc and the elastomer. Due to the characteristics of the elastomer which is transformed by the force, it is impossible to accomplish point contact between the elastomer and the lateral disc, and slippage is inevitable. Slippage not only degrades the efficiency of ElaCVT, but also causes wear of the elastomer resulting in performance variation. In order to observe
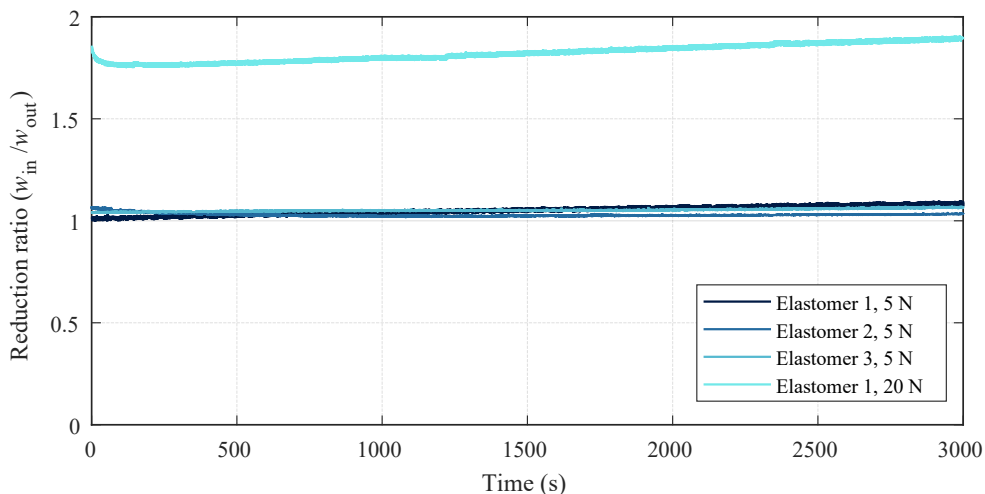
Figure 3.11: Variation of Reduction ratio of ElaCVT

the performance variation of the ElaCVT in the long-term usage, the reduction ratio of ElaCVT according to the driving time was observed under the fixed load and input velocity condition.

Figure. 3.11 shows the variation of the reduction ratio when the external forces were 5N and 20N, respectively. In each case, newly manufactured elastomers were used. The experiment was run continuously for 3000 s. Although the variation patterns of the reduction ratio at the beginning of the experiment was different depending on different elastomers, it was possible to observe a tendency for the reduction ratio to increase as the driving time increased. An increase in the reduction ratio in ElaCVT means that the contact points moved to a region where the radius of the lateral disc was shorter. During 3000 seconds, the reduction ratios of ElaCVT were reduced by less than 10%. When converted the change of reduction ratios to the change of the radius of the lateral disc, the change of radius was less than 0.2 mm.

During the 3000 s the continuous operation experiment, the total rotation amount of ElaCVT was 1,570,800 rad, which is enough to fully flex the proposed robotic finger over 5000 times. The contact point of ElaCVT changes according to the external force acting on the finger, and wear of the elastomer occurs on the overall surface of it unlike the experiment condition where the contact point was fixed. And it can be expected that the performance of the ElaCVT maintains for a longer period of time. However, performance degradation of ElaCVT cannot be avoided through long-term use of ElaCVT, and ultimately, further study is necessary to improve durability of ElaCVT.

Table 3.2: The specifications of ElaCVT-TSA and each component

Component Name	Motor with encoder Maxon, EC-max 16	ElaCVT	TSA	ElaCVT-TSA
Diameter	16mm	24 mm	1 mm (2×0.5 mm)	24 (maximum value)
Length	31 mm	27 mm	115 mm (including a string connector)	173 mm (58 mm without strings)
Weight	39 g	12 g	< 1 g	52 g
Power capacity	5 W	-	-	5 W
Nominal speed	5840 rpm	-	-	-
Nominal torque	3.23 mNm	-	-	-
Reduction ratio	1 : 1	1 : 1~2.31 : 1	16776 : 1 *	16776 : 1 $\sim$ 3811 : 1 *
Maximum continuous contraction Speed	-	-	-	0.037 m/s **
Maximum continuous contraction Force	-	-	-	(20 N) ***

* Reduction ratio of TSA represents [Input rotational speed (rad/s) : Output linear contraction speed (m/s)].
  The reduction ratio of TSA is average value along contraction length from 0 cm to 4.8 cm.

** Maximum continuous contraction Speed is calculated as multiplying the reduction ratio and nominal speed of the motor.

*** The hardware broke down before reached the Maximum continuous contraction Force. The value is the maximum external load we tested.

3.4.5 Specifications and Limitations of ElaCVT-TSA

The specifications of the ElaCVT-TSA manufactured in this study, and other elements are summarized in Table 3.2. This includes the string and connector of length 115 mm, and the total length of the ElaCVT-TSA recorded as 173 mm. Furthermore, the total weight of the ElaCVT-TSA is 52g. The reduction ratio of the TSA was expressed as the ratio of the input rotational speed and the output shrinkage speed, and, the average reduction ratio was calculated using the average speed during the contraction to 4.8 cm. The final reduction ratio from the motor speed to the contraction speed of the ElaCVT-TSA was passively and continuously varied from 16776:1 to 38811:1 according to external forces, and the maximum contraction force could not be measured due to the breakdown of the connector between the elastomer and output shaft.

The ElaCVT-TSA was fabricated and verified using a fused deposition modeling 3D printer using a PLA filament. However, some limitations should be improved to apply this concept to a wide range of areas. The first is the use of more rigid materials like aluminum, using which small and strong structure can be designed. In this study, the maximum contraction force of the ElaCVT-TSA was not able to be evaluated, because it broke down before reaching the maximum contraction force. Furthermore, the relatively large size of the ElaCVT devaluates the advantage of using small motors.

Second, the current design of the ElaCVT does not enable to utilize the maximum specifications of the motor. The maximum no-load speed of the motor, EC-max16, used in this study was 13500 rpm, but the maximum input speed of ElaCVT was about 9090 rpm. Moreover, the ElaCVT has lower efficiency compared to commercially available gearboxes. Thus the efficiency of

the ElaCVT was about 50%. Several losses were caused by a poor precision structure including 3D printed spur gears and friction generated by the TSA.

Third, as described in Section II, it is necessary to change the reduction ratio by 4 times to cover the operating region of the muscle efficiently. However, this study was only able to reached 2.31 times. Additionally, slippage was observed between the elastomer and the lateral disc when more than 3.3 mNm torque was applied. Also, a belt dressing was applied between the elastomer and the lateral disc to increase friction, but this does not constitute a fundamental solution. In this study, silicon was used to the test elastomers of different stiffnesses. However, silicon, as a material, does not have high friction characteristics. Therefore, further studies concerning the material and shape of the elastomer are needed to increase the amount of reduction ratio change and maximum transmittable torque.

Chapter 4

ANTHROPOMORPHIC ROLLING CONTACT JOINT

4.1 INTRODUCTION: COMPLIANT JOINT

As robotics has advanced, people encounter an increasing number of robots in various fields of daily life. Unlike gigantic industrial robots that are used in a space separated from humans, small manipulators have recently been developed for multiple tasks and directly cooperating with people. However, what the manipulator can perform is determined by what the end-effector can do because it is the gateway that directly interacts with the surrounding environment or objects. Unlike various commercially available manipulators that are similar in shape and specification with six or seven degrees of freedom, most end-effectors are designed based on a task to be performed. Therefore, even if a general-purpose manipulator is used, only the work targeted by the end-effector can be performed.

To conduct various tasks in human-centered environments, an end-effector with the performance, size, and weight of a human hand can be considered ideal. Although many studies have developed end-effectors, to overcome these lack of performance, human-hand-level end-effectors have not yet been developed. [44].

Recently, various end-effectors using soft materials, such as silicone, have been studied. The flexibility of the material enables the gripper to interact with the surrounding environment and objects actively, and this adaptiveness makes it possible to stably grasp various objects by compensating for the low degrees of freedom or lack of sensors. Compared with conventional rigid grippers, which are capable of adaptive grasping only in the joint driving direction, soft grippers can grasp objects more stably with passive shape deformation [55].

Manti et al. designed soft grippers with three fingers using two types of silicone [56]. This soft gripper uses only one tendon-driven actuator, but it shows that stable grasping postures are accomplished regardless of the shape of the objects using the compliance of silicone and the adaptive mechanism of each finger. Furthermore, studies have been conducted to grasp objects using the fingertips of soft grippers with multiple actuators for one finger. Zhou et al. showed that a three-finger soft gripper with six degrees of freedom can handle a small object using the fingertips, in which cylindrical bumps were applied [57]. Teeple et al. designed a soft finger comprising two parts and experimentally analyzed the success rates of power grasping and pinch grasping based on the ratio of the two parts [58]. However, precise control of soft grippers compared to grippers consisting of rigid materials (plastic, aluminum, steel, etc.) still remains a big challenge.

To compensate for the shortcoming of soft grippers, various hybrid-type
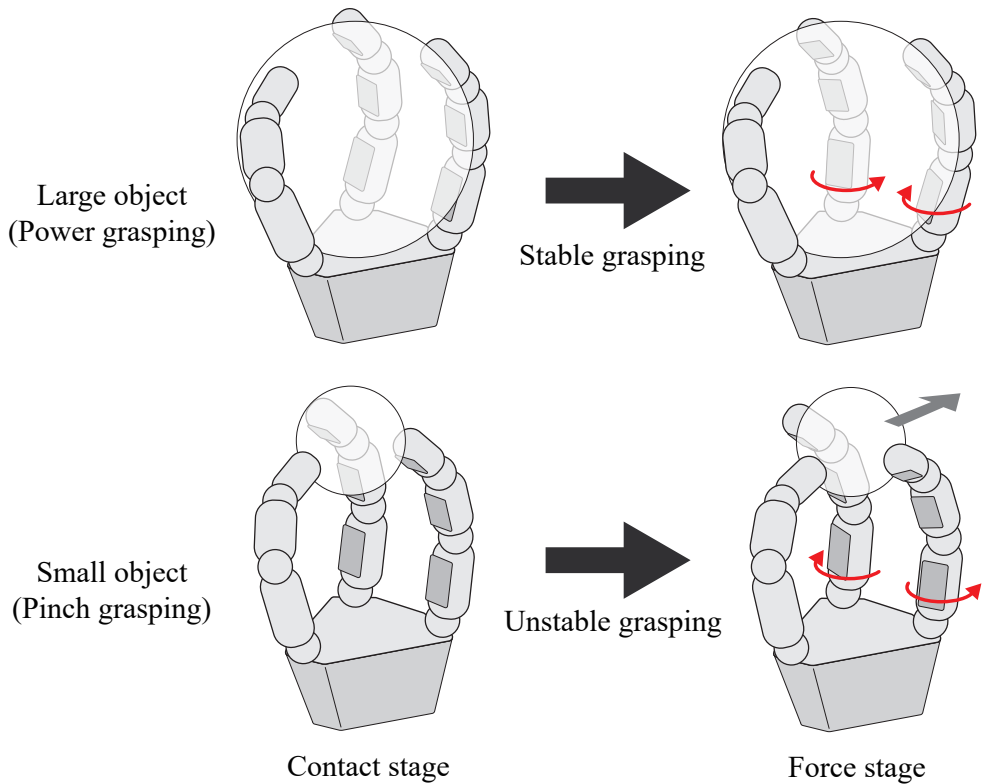
Figure 4.1: Influence of joint compliance when grasping a large object and small object. The small object can be ejected from the fingertips due to the changes in fingertip position.

grippers have been developed, whose bones consist of rigid materials but joints consist of soft material, such as urethane joints and rolling contact joints with elastic ligaments [13][59][60][16].

However, the fact that each joint can adapt to external forces implies that the fingertip position cannot be maintained at the desired position when contact occurs on the end-effectors. As shown in Fig. 4.1, in power grasping, the surfaces of each phalange are in close contact with the surface of an object, which improves the grasping stability. However, when grasping using the fin-
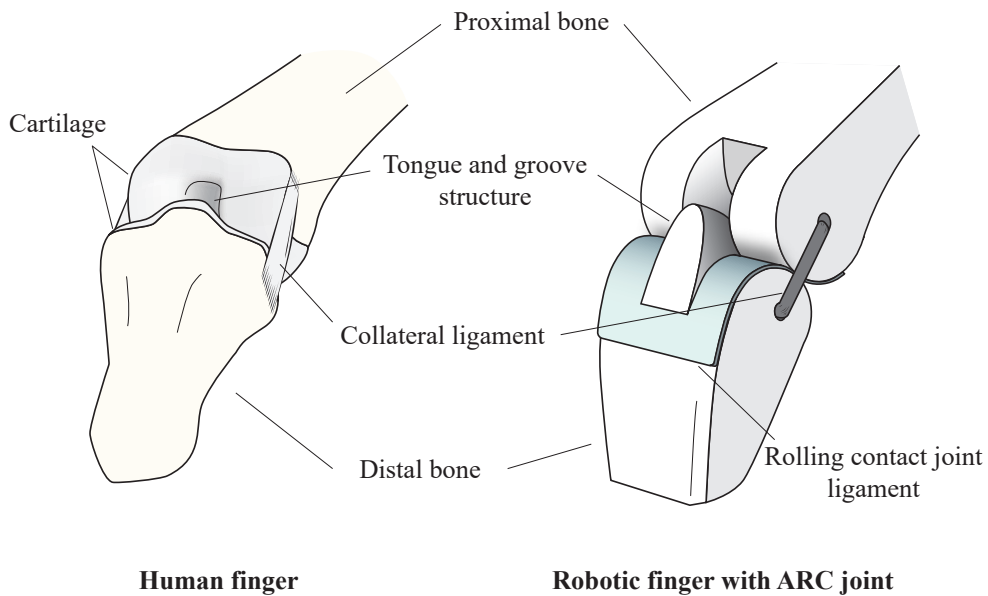
Figure 4.2: Comparison between components of human finger joint and ARC joint. The structure of the ARC joint was inspired by contact surface shapes and collateral ligament of the finger joints. The left shows distal interphalangeal joint of human finger, and the right shows the proposed ARC joint

gertip, such as pinch grasping, the objects are ejected between the fingers, and the grasping success rate decreases because of changes in the fingertip position. Various studies related to adjusting joint compliance have been conducted, but the mechanisms require additional size and weight of the end-effectors.

Human joints actively control the stiffness of a joint by using ligaments constituting the joint and surrounding muscles, and if joint stiffness can be actively adjusted, the aforementioned limitations can be improved. Zhu et al. analyzed the joint structure of human fingers and proposed a highly biomimetic joint that realize musculoskeletal characteristics [61][62]. However, because of complex structure of the joint that is difficult to manufacture and customize, the highly biomimetic joint is applicable only to limited robotic systems like

robotic hand [63] [64].

In this study, a novel compliant rolling contact joint, an anthropomorphic rolling contact joint (ARC joint) was proposed, whose torsional stiffness passively increases according to the joint angle to realize low joint stiffness in power grasping and high joint stiffness in pinch grasping without additional weight and size. The ARC joint mimics the structures of the human finger joint, tongue-and-groove, and collateral ligaments, improving the structure of the existing rolling contact joint, and Fig. 4.2 shows a comparison between the human finger joint and ARC joint.

The remainder of this paper is organized as follows. In Section 4.2, we introduce related studies on rolling contact joints. Section4.3describes the detailed design structure, including the differences between the previous rolling contact joints and ARC joint. The experimental results of the joint stiffness of the ARC joint are presented in Section 4.4. In Section V, the functionality of the ARC joint is experimentally demonstrated by applying the ARC joint to two different three-finger robotic grippers.

4.2 RELATED WORKS: ROLLING CONTACT JOINT

According to a patent proposed by Hillberry, the basic structure of the rolling contact joint is illustrated in Fig. 4.3(a). Two ligaments intersect and connect to each bone, and because of the constraint that the length of the ligaments is maintained, the surfaces of both bones can roll without slipping [65]. Compared with the revolute pin joint, the rolling contact joint has the following advantages. First, it can withstand a stronger force than to a pin joint in a
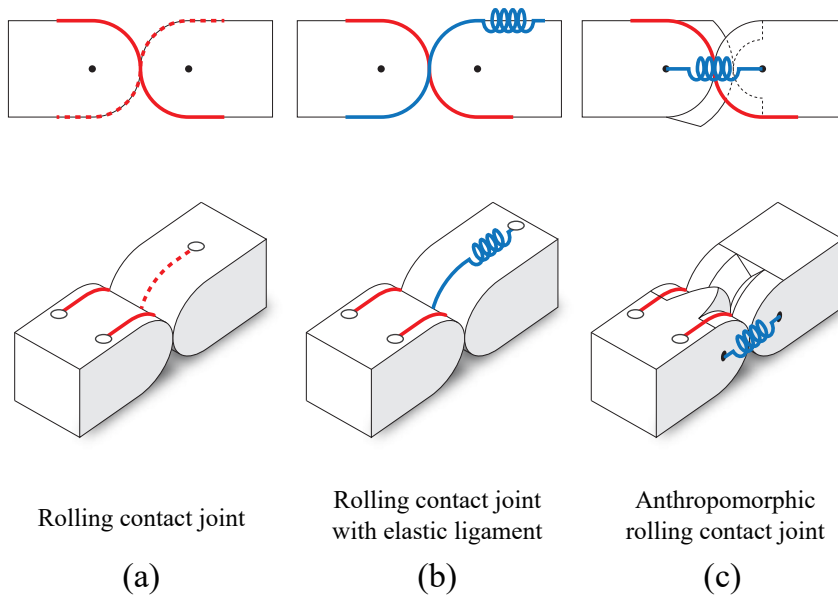
Figure 4.3: Diagrammatic comparison between Rolling Contact joints, (a) Conventional rolling contact joint, (b) Rolling contact joint with extensible ligament, (c) Anthropomorphic rolling contact joint. Red lines represent inextensible tendon, and blue ones represent extensible tendon.

compact structure [66]. This is because the ligament supports the tensile force and the bone supports the compressive force. Second, it is possible to manufacture them inexpensively because expensive parts, such as bearings, are not required. Third, it has a wide range of motion by avoiding self-collision compared to the pin joint. Because of these characteristics, the rolling-contact joint has been applied to various end-effectors, such as grippers and robotic hands, including an artificial implant joint [67][68].

However, the rolling contact joint has limitations. First, the performance of the joint is guaranteed only when the two ligaments are fixed exactly in the correct position on the two bones. If the length is slightly longer, a gap occurs between the two bodies, such as the backlash of gears, and if the length

is short, assembly becomes impossible. Second, it cannot compensate for any ligament stretching that occurs during the actual operations. If the ligament is stretched owing to external impact or repeated use, the aforementioned problem occurs. However, because the ligaments of the rolling contact joint are installed between the bones and cross each other, replacing the ligaments requires more effort than repairing the pin joint.

To complement the limitations, various types of rolling contact joints with compliant material have been studied [59][16][69]. Kim et al. proposed a rolling contact joint in which an elastic element is applied to one of the two ligaments, as shown in Fig. 4.3(b) [13]. With this compliant ligament, the rolling contact joint can not only absorb the impact force acting on the finger and prevent damage, but also compensate for the elongation and manufacturing error of ligaments. By designing different pulley radii for the proximal and distal bones of the elastic ligament, a passive extension force without additional mechanisms was implemented. However, the joint compliance caused by the application of an elastic ligament to the rolling contact joint has not been analyzed, and there are no previous studies related to effect on object grasping stability.

4.3 ANTHROPOMORPHIC ROLLING CONTACT JOINT

In this section, the structure of the ARC joint and its fundamental working principle are introduced. Next, the advantages of the ARC joint are discussed.
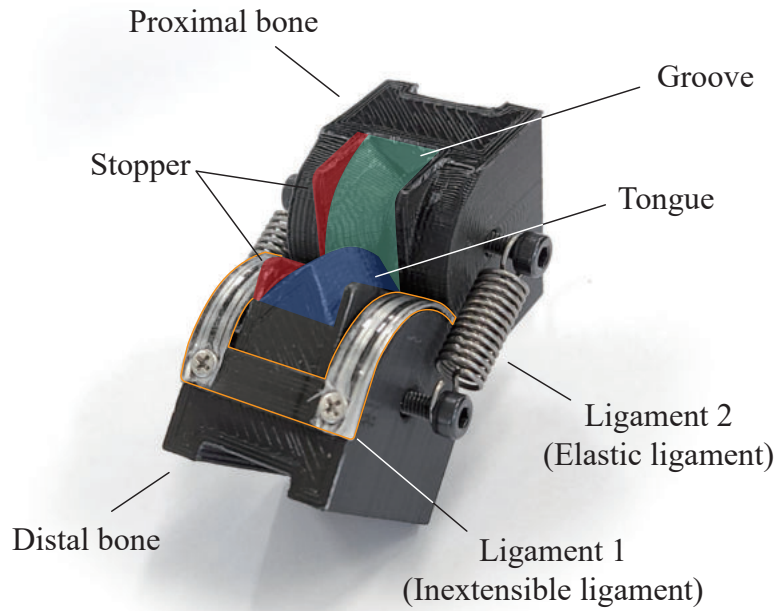
(a)
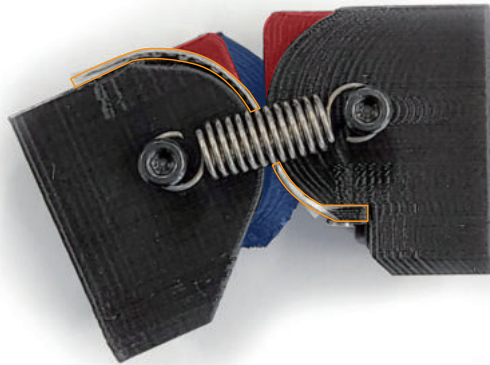
(b)

Figure 4.4: Details of manufactured ARC joint, (a) Component name of ARC joint in perspective view, (b) Lateral view of ARC joint
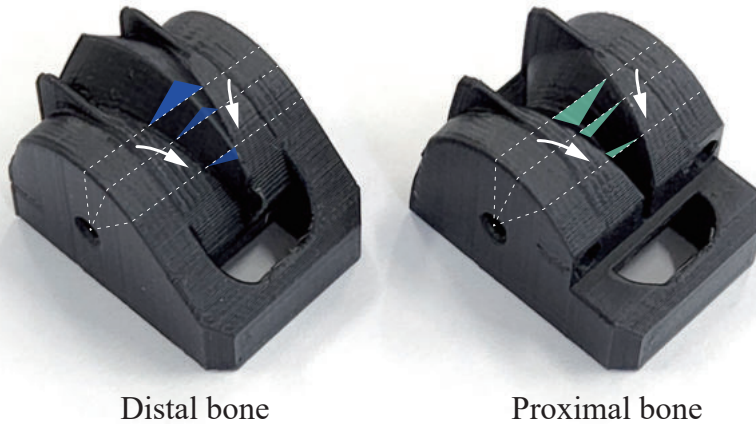
Figure 4.5: Example shape of tongue-and-groove. To reduce the number of required ligaments, the shape should be narrowed in the direction of the arrow

4.3.1 Fundametal Components of ARC joint

The ARC joint mimics the two components in human finger joints, the tongue-and-groove mechanism, and collateral ligaments; these are known to improve joint stability [70][71]. Fig. 4.4 shows the detailed structure of the ARC joint, and the colors on each component were overlaid for better visibility. Similar to human joints, grooves (green) and tongue (blue) are designed on the contact surface of the proximal and distal bones, and two types of ligaments are used to constrain these two bodies. These two ligaments have opposing properties. Ligament 1 (orange) is located between these two bodies and prevents slipping on the surface of each bone and should be manufactured using an inelastic material. Conversely, Ligament 2 should have elasticity for joint compliance and is located beside the two bones, similar to collateral ligaments in the human joint finger (Fig. 4.2). Unlike the elastic ligament of previous rolling contact joints (Fig. 4.3(b)), Ligament 2 of the ARC joint can only compensate for the

short Ligament 1, and elongation of Ligament 1 causes backlash. In addition, a stopper was placed beside the tongue and groove to prevent hyperextension.

In this study, commercial springs were used as Ligament 2; however, various elastic materials can be applied. When torsional rotation occurs in the ARC joint, the distance between the centers of the two bodies increases, and Ligament 2 exerts a restoration force owing to the interference of the tongue-and-groove structure. Therefore, the elastic modulus of Ligament 2 should be determined by considering the purpose of the joint.

Fig. 4.5 shows an example of the shape of the tongue and groove. One of the most important design features of the ARC joint is that the shape of the tongue and groove of the ARC joint should be narrowed in the direction of the arrow (white arrow in Fig. 4.5) to reduce the number of required ligaments located between the bodies. Without this characteristic, the joint could not resist the $+y$ displacement of the distal bone (Table. 4.1). The interference between the wide tongue and narrow groove elongates the collateral ligament when a $+y$ displacement occurs. In the case of humans, there is a slight difference between the shape of the tongue and groove but the same shape was applied in this study [72].
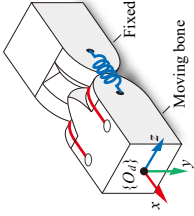
The linear and angular stiffnesses along each direction were determined differently from those of the conventional rolling contact joint. The components that determine the stiffness in each direction are shown in Table. 4.1. The relative displacements of the distal bone are expressed in the coordinates of the distal bone, O_d. Most stiffnesses are determined by the elastic coefficient of Ligament 2 and the shapes of the tongue and groove. However, the linear stiffness along $-x$ and $-y$ is determined by the material properties of bones

and Ligament 1, respectively. In most cases, these are much larger than the stiffnesses of the other directions. This is because the bones are made of a rigid material, and Ligament 1 has inextensible properties.

This difference between the stiffnesses in the positive and negative y-directions is the main reason why we selected the bone with a groove as the distal bone of the finger joint. In most object grasping situations, the forces acting perpendicular to the bottom surface of the bone ($+y$ direction) are reaction forces from the grasped object. Therefore, for firm grasping, the joint should resist the force that does not conform.

One of the advantages of rolling contact joints is that the z-direction rotational stiffness and friction are zero because there is no slip between the surfaces. Ideally, the z-direction rotational stiffness of the ARC joint is also zero, but because of the slip between the surfaces of the tongue and groove friction occurs when the joint is rotated. Therefore, in applications where little friction is required and no lateral force or twist torque exists, the conventional rolling contact joint will be more suitable than the ARC joint. However, in applications that need to adapt to external forces in various directions, such as robotic fingers, the ARC joint has advantages.

Table 4.1: Components that determine linear/angular stiffness along each direction

Direction of displacements of distal bone	Linear stiffness	Angular stiffness
$+x$	Elastic coefficient of collateral ligaments	Elastic coefficient of collateral ligaments and shape of tongue and groove
$-x$	Material property of bones	
$+y$	Elastic coefficient of collateral ligaments and shape of tongue and groove	Elastic coefficient of collateral ligaments and *partially* shape of tongue and groove
$-y$	Material property of ligament	
$+z$	Elastic coefficient of collateral ligaments and shape of tongue and groove	Ideally zero stiffness
$-z$		

4.3.2 Advantages of ARC joint

The first advantage of the ARC joint is that its stability is improved. With the collateral ligament, stability against torsional twist, as described above, as well as stability against translation in the x, y, and z directions, and rotation in the y direction is significantly increased. These values can be modified by adjusting the shape parameters of the ARC joint, including elastic modulus of the collateral ligament and tongue-and-groove shape. In particular, it has the advantage of being able to express the desired characteristics according to design parameters, unlike previous studies that eliminated compliance in a specific direction by using a gear shape to overcome the problems of the existing rolling contact joint.

Second, the ARC joints have advantages in terms of manufacturing. The ARC joint can be reassembled after a complete disassembly, and the reduced number of ligaments that pass between the bones from two to one makes it easier to design and assemble. This is because, unlike other rolling contact joints that use knots or adhesives to fix ligaments to bones in the manufacturing process, ligaments of ARC joints can be fixed using screws and can be disassembled without damage. As a result, the use of ARC joint not only allows for easy maintenance but also significantly reduces the error in joint performance that can occur depending on the skill of the assembler.

LM guide 1

Joint angle

Actuator 1
(ROBOTIS, XM430-W350-T)

ARC joint

z y

x

Twist angle

LM guide 2

LM guide 3

Force/Torque Sensor
(ATI, AXIA80-M20)

Actuator 2
(ROBOTIS, XM430-W350-T)
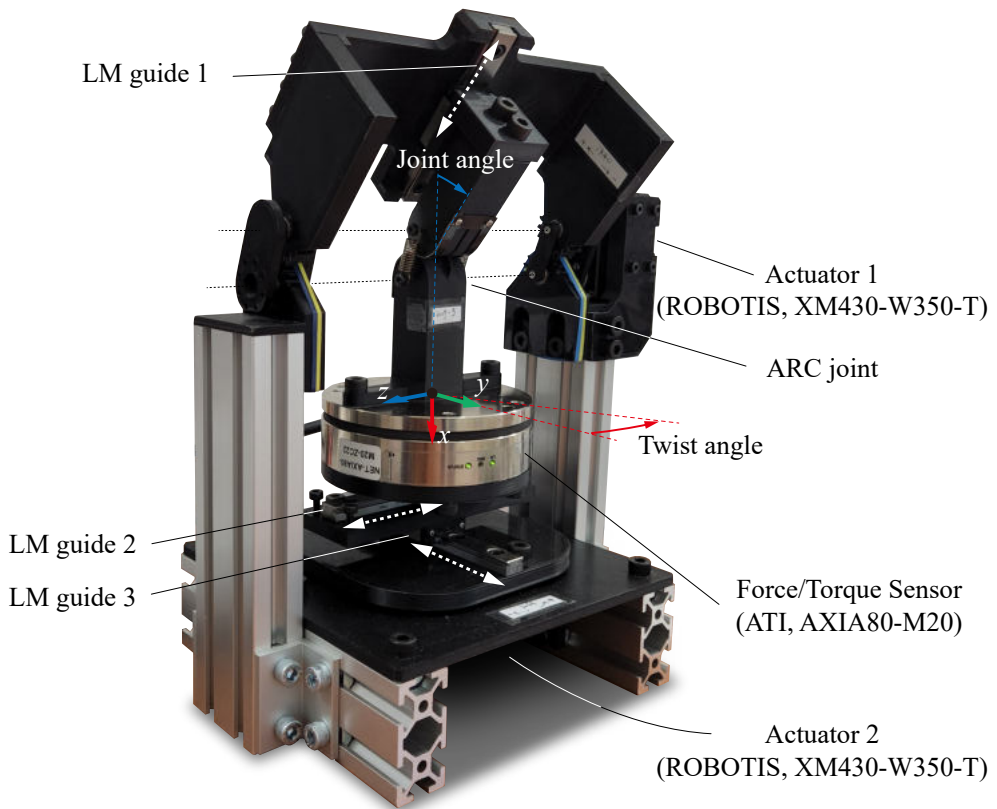
Figure 4.6: Experimental setup to evaluate torsional stiffness ARC joints

4.4 TORSIONAL STIFFNESS EVALUATION

4.4.1 Experimental Setup

Fig. 4.6 shows the experimental setup used to measure the torsional stiffness of the ARC joints at various angles of the joint. Using two actuators (ROBOTIS, XH430-W210-T), the torsional stiffness could be measured without human interference, after the test subject was installed. Actuator 1 changes the joint angle (q) of the ARC joint, and actuator 2 adjusts the twist angle (θ_{twist}) of the distal bone. The motion of each actuator is shown in Fig. 4.6 with blue and red arrows. A force/torque sensor (ATI Industrial Automation, AXIA80-M20) was installed between actuator 2 and the distal bone to measure torque in the vertical direction.

The twist movement of actuator 2 generates relative motion between the two bones. First, torsion causes interference between the tongue and groove structure, thereby increasing the distance between the two bones. The second relative motion is generated in the yz-plane in Fig. 4.6 because of Ligament 2. Depending on the rotational direction of the proximal bone, slack occurs on one side of Ligament 1 and a tensile force acts on the opposite side. Owing to the inextensible characteristic of Ligament 1, the rotational center of the proximal bone should be located on Ligament 1, not on the center of the bones. Considering the influence of these relative motions, three linear motion guides (LM guides) were installed in the experimental setup. The locations and movement directions of each LM guide are shown in Fig.4.6.
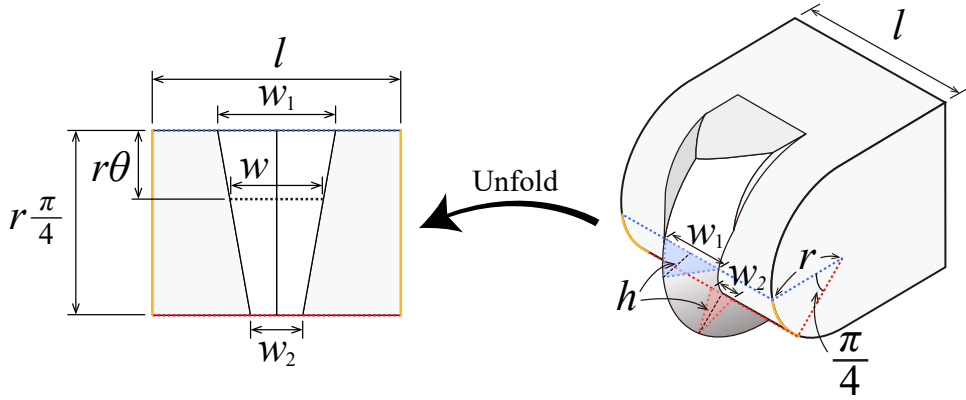
Figure 4.7: ARC joint design parameters of proximal bones. In this study, the ARC joints had triangular tongue and groove shape with identical height. Left figure shows unfolded contact surface from $\theta = 0$ to $\theta = \pi/4$.

Table 4.2: Dimensions of six ARC joints with different tongue and groove shapes and a joint without tongue and groove shape

Name	r	l	h	w_1	w_2
w7-6					6 mm
w7-5					5 mm
w7-4.5					4.5 mm
w7-4	10 mm	20 mm	4 mm	7 mm	4 mm
w7-3.5					3.5 mm
w7-3					3 mm
w0-0				0 mm	0 mm

4.4.2　Design and Manufacturing of ARC joints

Fig. 4.7 shows the design parameters of the ARC joint, and Table. 4.2 shows the dimensions of the ARC joints used in this experiment. The radius (r) of the contact surface was 10 mm and the width (l) of the two bones was 20 mm. Each dimension is determined by considering the size of the robotic fingers. In this study, a triangular shape was applied to evaluate the influence of different shape of tongue and groove mechanism. The height (h) and width (w_1) of the tongue and grooves at 0° were fixed at 4 mm and 7 mm, respectively. Six different ARC joints were manufactured with different w_2, widths at 90°, from 3 mm to 6 mm. The w value according to the angle was linearly interpolated using Equation (4.1).

$$w(\theta) = w_1 + \frac{4\theta}{\pi}(w_2 - w_1) \tag{4.1}$$

To achieve manufacturing repeatability of the joint, the bones of the ARC joints and Ligament 1 were manufactured using an FDM-type 3D printer (Ultimaker S5) with tough polylactic acid (PLA). The ligament produced through 3D printing allows it to be combined in a more precise position than the conventional method using a string. The disadvantage of this method is that ligaments made of PLA are vulnerable to repeated flexion. To improve this problem while maintaining the simplicity of fabrication fiberglass tape was applied on both sides of the ligament. Two commercial springs were used for Ligament 2; the free length, spring coefficient, and initial tension were 18.1 mm, 0.99 N/mm, and 2.501 N, respectively.
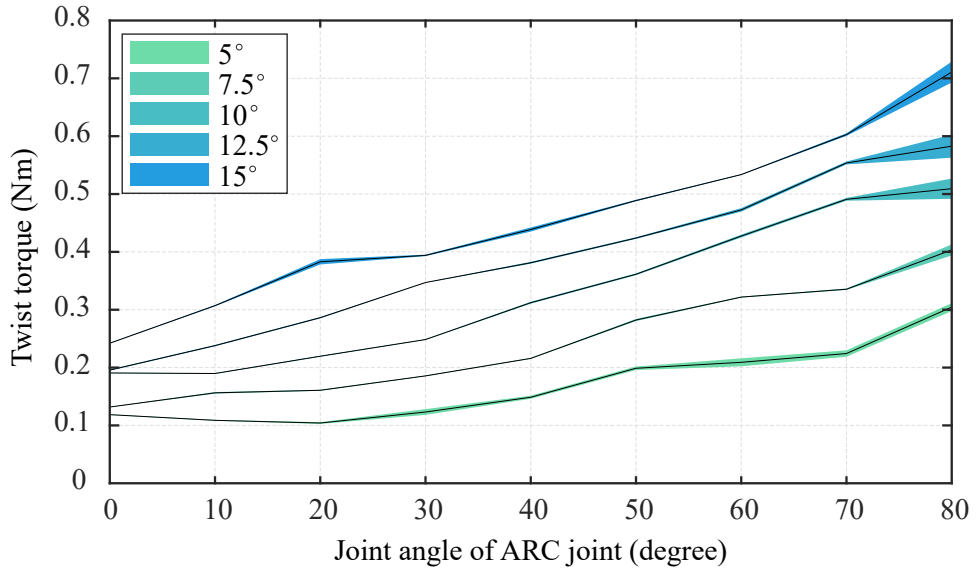
Figure 4.8: Average twist torque of w7-3 under different twist angles
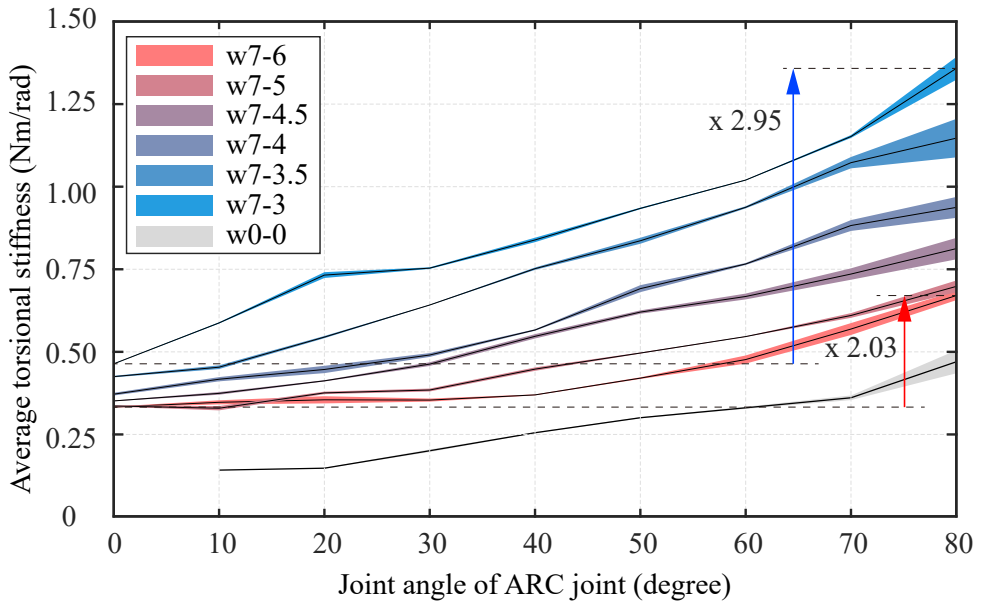
Figure 4.9: Average torsional stiffness of ARC joint under 15° twist angle

4.4.3 Torsional Stiffness Change according to Joint Angle and Twist Angle

In this study, to evaluate the stiffness characteristics of the ARC joint, the torsional torque (τ_z) was measured by the force/torque sensor when twisted by θ_{twist} in both directions. The average torsional stiffness (S) was calculated by dividing the sum of the absolute values of the torques by the total amount of twist ($2 \cdot \theta_{twist}$), as shown in Equation (4.2). The average torsional stiffness was estimated for various joint angles and twist angles using different ARC joints with the dimensions listed in Table. 4.2.

$$S = \frac{|\tau_{+x}| + |\tau_{-x}|}{2 \cdot \theta_{twist}} \tag{4.2}$$

Fig. 4.8 shows the twist torques ($|\tau_{+x}| + |\tau_{-x}|$) of w7-3 ARC joint. Experiments were conducted from 0° to 80° at 10° intervals, and the twist angle varied from 5° to 15° at intervals of 2.5°. The measurements were repeated 5 times in all cases. The solid black lines represent the average of five measured values, and each colored area represents $\pm\sigma$ (standard deviation) from the normal value.

The average torsional torque increased as the twist angle increased for all joint angles. However, it can be observed that there was a difference in the amount of change depending on the joint angle. The twist torque increased most linearly at a joint angle of 40°, and it was observed that the linearity decreases significantly as the joint angle approaches 0° and 80°.

Fig. 4.9 shows the torsional characteristics of the six ARC joints with different tongue-and-groove shapes (Table. 4.2). The average torsional stiffness was

measured in the same range of joint angles as those in the previous experiment. The experiments were conducted five times at a twist angle of 15° in all the cases. The solid line indicates the average value and the colored area indicates $\pm\sigma$ from the average.

In most cases, six different ARC joints had a tendency to increase torsional stiffness as the joint flexed, but in case of w7-6, the torsional stiffness from 0° to 40° was maintained. As w_2 decreased, the rate of change in torsional stiffness increased. Comparing the torsional stiffness at 0° and 80°, in the case of w7-3, it increased to 2.95 times (0.46 Nm/rad to 1.36 Nm/rad), while in the case of w7-6, it increased to 2.03 times (0.33 Nm/rad to 0.67 Nm/rad).

The results in Fig. 4.9 show that the torsional stiffness of the ARC joint is influenced not only by the instantaneous tongue-and-groove shape but also by the rate of shape change. Although the tongue and groove shapes of the six ARC joints used in the experiment were the identical at a joint angle of 0°, torsional stiffness increased as w_2 decreased. This is because the amount of interference between the two bones caused by torsion increased as $|\frac{\delta w}{\delta \theta}|$ increased.

4.5 TORSIONAL STIFFNESS WITH JOINT COMPRESSION FORCE DUE TO TNESION OF TENDONS

The main factors that cause torsional stiffness of the ARC joint are the shape of the tongue and groove and the collateral ligament. The tension of the collateral ligament caused by torsion of ARC joint generates the restoring force. The
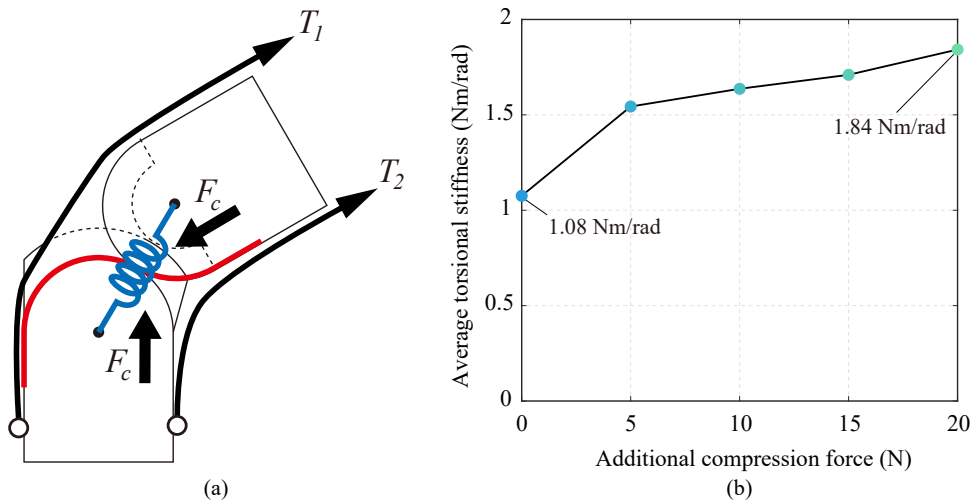
Figure 4.10: ARC joint with additional compression force, (a) ARC joint with two tendons acting antagonistically, (b) Average torsional stiffness of w7-3 ARC joint under different additional compression forces

stiffness of a human joint can actively be adjusted depending on the activation of the surrounding tendons and muscles, and this is because multiple muscles act antagonistically on one joint. Similarly, if the tendons around the ARC joint act antagonistically, the torsional stiffness of the ARC joint can also be actively controlled. Fig. 4.10(a) shows the ARC joint and two tendons passing around it. The two tendons act antagonistically, and by adjusting the tension T_1, T_2 of each, it is possible to increase the compression force, F_c, by compressing the joint without changing the joint position. The F_c acts as a restoring force whether or not the ARC joint is twisted as the force generated by the collateral ligaments.

Fig. 4.10(b) shows the change in torsional stiffness of the joint as the compressive force of the ARC joint increases. In this experiment, the w7-3 ARC joint was used. Using the experimental setup shown in Fig. 4.6, the experiment was conducted while changing the compressive force while joint angle was

fixed at 60°. The average torsional stiffness of the joint was measured as the experiments conducted in Fig. 4.9. The average torsional stiffness without any compression force was estimated 1.08 Nm/rad. However, the average torsional stiffness increased to 1.84 Nm/rad with the 20 N additional compressive force. The result shown that the torsional stiffness increased as the compressive force increased.

The robotic finger proposed in Section. 2.2 had three ARC joints, but each ARC joint had a difference in active torsional stiffness control ability according to the tendons passing through the joints. In order to actively control the torsional stiffness maintaining the joint angle, the tendons around the joint must actuate the joint antagonistically. In the MCP FE joint, the intrinsic and extrinsic tendons can control torsional stiffness actively acting antagonistically. However, the torsional stiffness of the PIP FE joint cannot be actively controlled without an external contact force, because both intrinsic tendons and extrinsic tendons had moment arms in the same direction (flexion) (Fig. 2.7).

4.6   TORSIONAL STIFFNESS
WITH LUBRICATION STRUCTURE

Unlike the rolling contact joint, the ARC joint generates friction between the tongue and the groove during joint flexion/extension and twisting, which cause abrasion and degrade joint performance. Fig. 4.11 shows Ligament 1 with a lubrication structure to reduce the friction between tongue and groove. A nitrile rubber tube containing teflon grease was combined with ligament 1 using fiberglass tape. In this study, Ligament 1 manufactured by 3D printer using
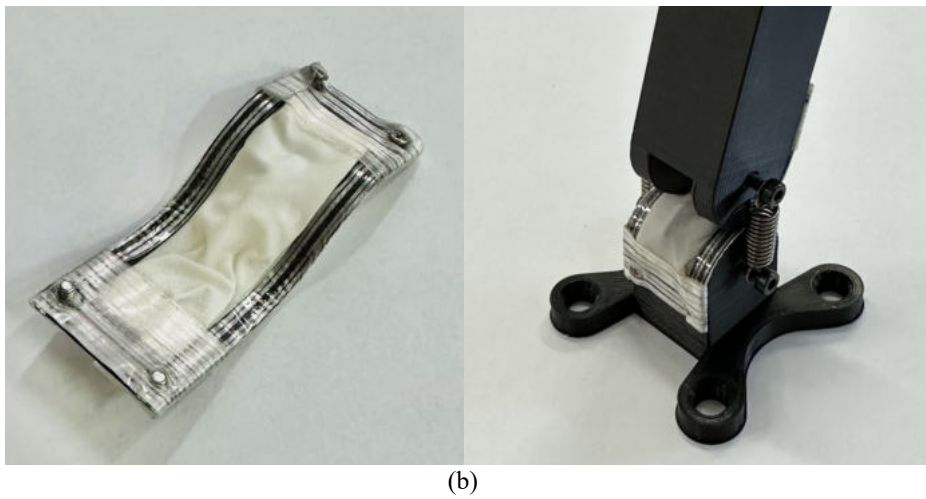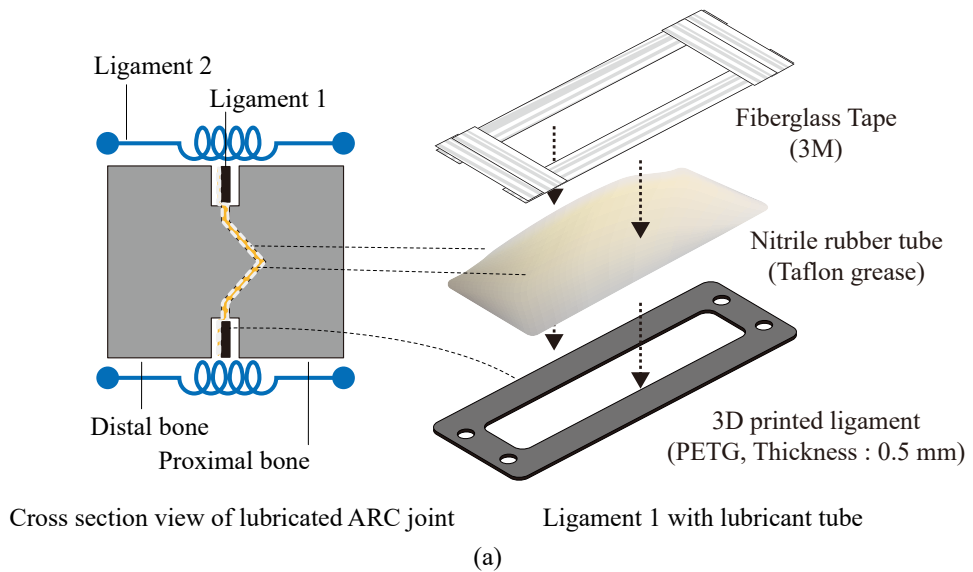
Figure 4.11: Ligament 1 with lubricant structure. (a) Detail components of Ligament 1 with lubricant tube, (b) Manufactured Ligament 1 with lubricant tube and lubricated ARC joint
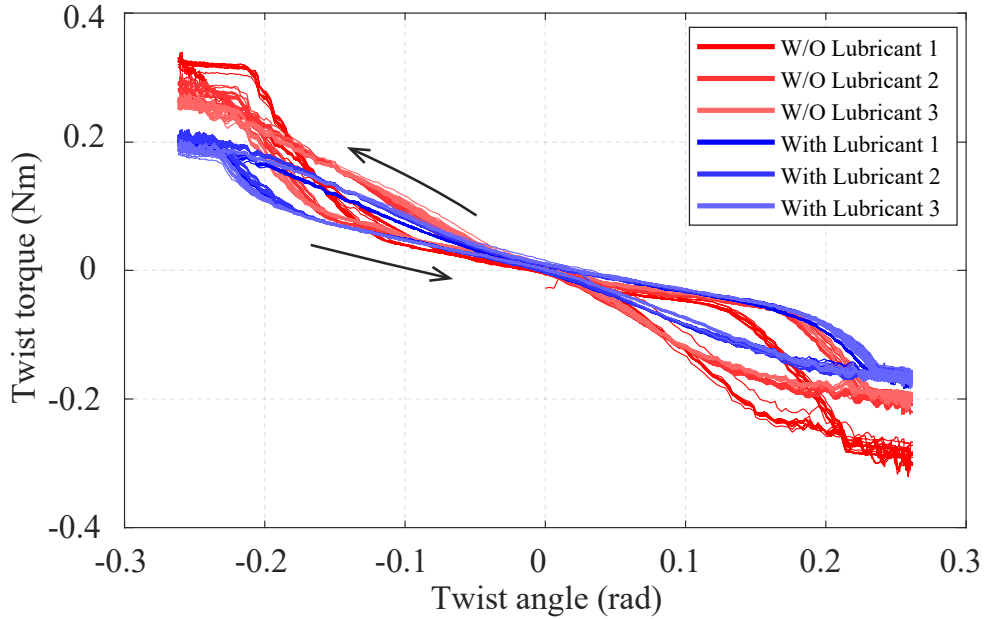
Figure 4.12: Twist toque of six w7-3 ARC joints at 60° joint angle with/without lubrication structure according to twist angle

tough PLA, and fiberglass tape complements the durability of Ligament 1. The proposed lubrication structure was completely sealed so that the teflon grease was not lost during the joint motion.

Fig. 4.12 shows the twist torque of six w7-3 ARC joints according to the twist angle at 60° joint angle. Red lines represent the twist torque of three w7-3 ARC joints without lubrication structure, and blue lines represent that of three w7-3 ARC joints with lubrication structure. The experiment results showed that the ARC joint with the lubrication structure not only measured a smaller maximum twist torque than the ARC joint without the lubrication structure, but also showed small performance differences between individuals.
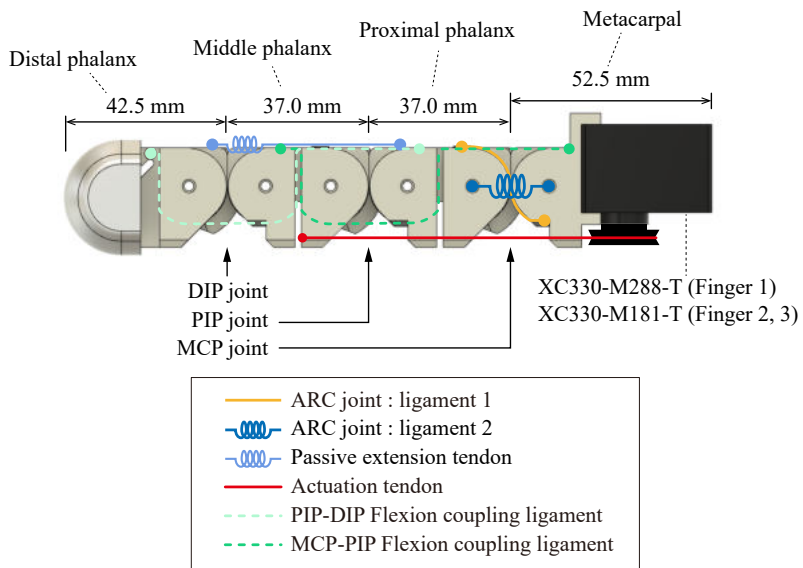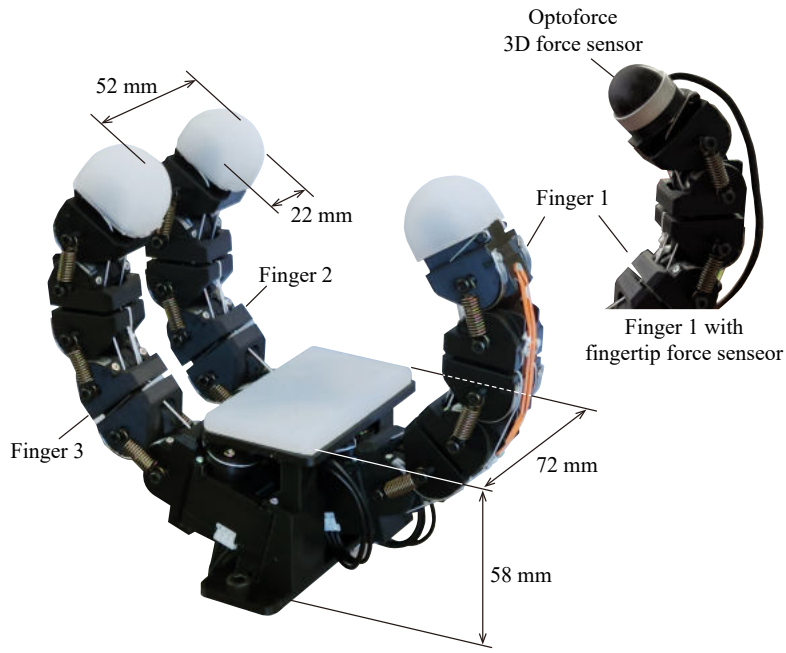
Figure 4.13: Detail of gripper and modular finger, (a) Overall design of the three-finger gripper, (b) Design and ligaments of fully extended modular finger. Ligaments related with ARC joint are representatively illustrated on MCP joint.

4.7 GRASPING PERFORMANCE COMPARISON OF GRIPPERS WITH DIFFERENT ARC JOINTS

To verify the effect of the ARC joint on the grasping process, we fabricated two three-finger grippers with different tongue-and-groove shapes (w7-6 and w7-3) and observed their grasping stability. When the ARC joint, whose stiffness increases according to the joint angle, is applied to the robot finger, it is possible to stably pinch grasp a small object by utilizing high joint stiffness. Simultaneously, stable contact with an object or environment is feasible in the early stage of grasping with stretched fingers.

Fig. 4.13(a) shows a three-finger gripper with ARC joint, and Fig. 4.13(b) shows the structure of a single modular finger. The gripper consists of Finger 1, Finger 2, and Finger 3, facing each other. The distance between Finger 2 and Finger 3 was 52 mm considering the width of the modular finger (22 mm), and Finger 1 was located in the middle of Finger 2 and Finger 3. The force sensor (Optoforce, 3D force sensor) could be attached to the distal phalange of Finger 1 to measure the contact force while grasp objects. The total weight of the gripper was estimated at 291 g. The three fingers were designed with the same structure except for the actuator. Finger 2 and Finger 3 were actuated by XC330-M181-T from ROBOTIS, and Finger 1 was actuated by XC330-M288-T, which has a higher reduction ratio than XC330-M181-T. This is because Finger 1 must withstand the force of the two opposing fingers in the process of grasping an object. The maximum fingertip force exerted by finger 1 with 30° joint angle of MCP, PIP, and DIP FE joints was 2.2N, and the maximum fingertip force of Finger 2 and 3 , which have lower reduction ratio, under the same posture was 1.3 N. The maximum fingertip forces were estimated with

600 mA motor current.

The finger consists of four links (metacarpal, proximal phalanx, middle phalanx, and distal phalanx) and MCP, PIP, and DIP joints. The three joints had the same structure as the ARC joint used in the previous experiment (Fig. 4.4). Three identical ARC joints were driven by an actuator using a tendon-driven mechanism. In free motion, all three joints were actuated identically owing to the two coupling ligaments. Because the actuating tendon was fixed to the middle phalanx, it enabled adaptive grasping by actuating the DIP and PIP joints even when contact occurred on the proximal phalanx. A silicone cover (Shore 40A) was applied to the fingertips and palm of the gripper to improve grip stability.
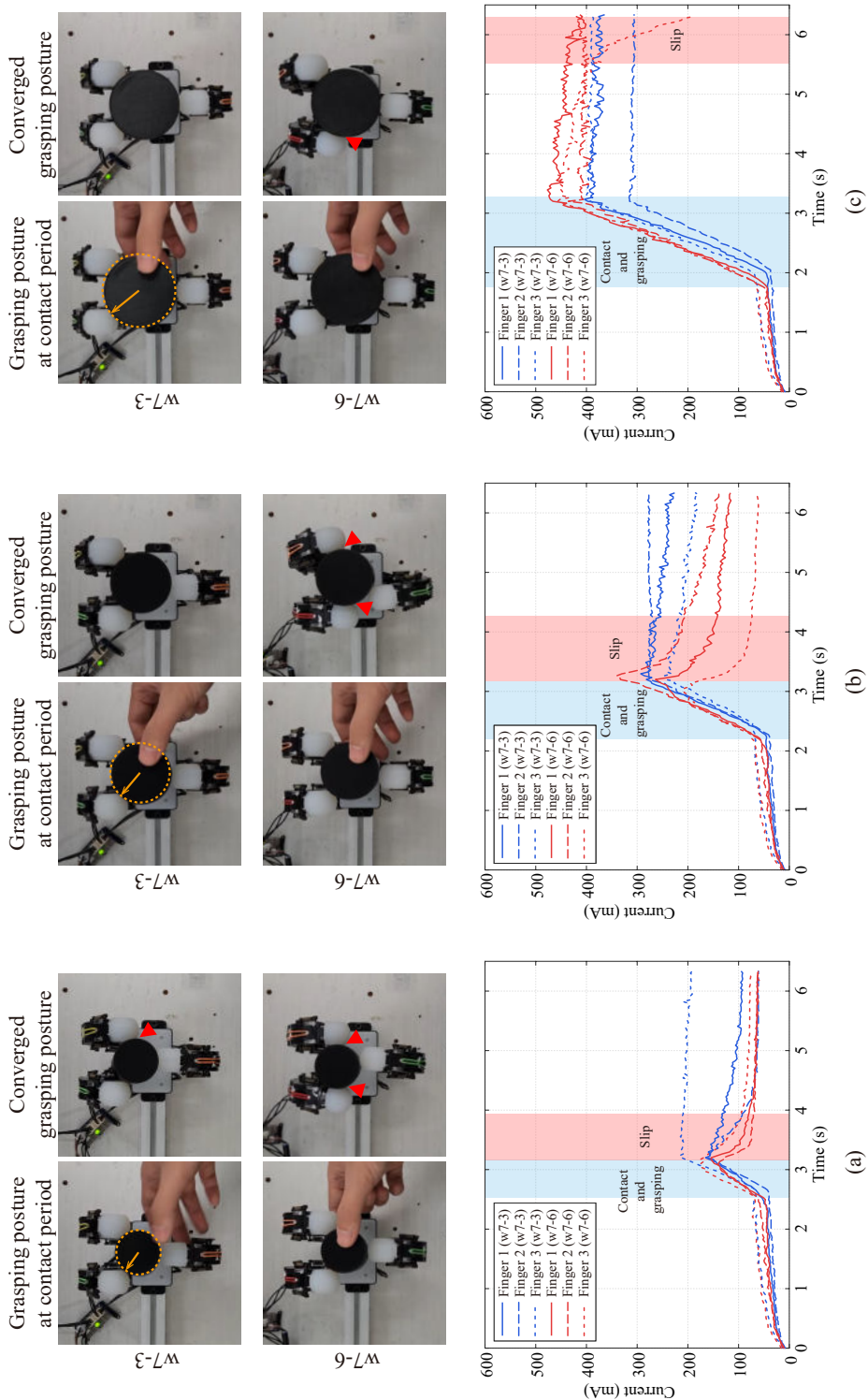
Figure 4.14: Grasping postures (top view) and actuator currents of each finger during grasping a cylinder-shaped object with different diameters, (a) 40 mm diameter, (b) 50 mm diameter, (c) 60 mm diameter. More slip occurred in the gripper composed of arc joint of w7-6 with low torsional stiffness. The motor currents dropped when slipping occurred.

Fig. 4.14 shows the results of the grasping experiment using two different grippers. For the experiment, cylinders with three different diameters of 40 mm (Fig. 4.14(a)), 50 mm (Fig. 4.14(b)), and 60 mm (Fig. 4.14(c)) were used. The above pictures show the grasping postures when contact between the object and the fingertip occurred and the final converged grasping postures in each case. The graphs below show the instantaneous current values of each finger during the object-grasping process. With the current graphs, the status of the fingertips could be analyzed because the currents were controlled to be proportional to the position error. In the process of grasping the object, the desired positions of the actuators were designed to flex the finger at a constant speed, which implies that if contact with an object occurs while flexing the finger, the position error and input current increase. Conversely, when a slip occurs between the object and the fingertip, the current value drops rapidly. In the graphs, blue lines represent the currents of the finger with the w7-3 ARC joints, and the red lines represent the currents of the finger with the w7-6 ARC joints. It was observed that the current value of the fingers gradually increased before contact occurred because the passive extension tendon extended as each finger flexed.

Although a silicone cover with a sufficiently large friction coefficient was applied to the fingertips to increase the grasping stability, the gripper with w7-6 ARC joints caused slippage between the object and the fingertips in all experiments.

The smaller the diameter, the larger the slip was observed. As the diameter of the object decreased, the direction of the reaction force (orange arrows in Fig. 4.14) transmitted from the object to the fingertips became more horizontal. Each finger can only control the vertical force, and the horizontal force is

determined by the stiffness of the joint and the amount of deformation of the fingertip position. As the object becomes smaller, the joint angle at the contact period increases, which not only increases the joint stiffness, but also the reaction force in the horizontal direction. The horizontal component of the reaction force increases rapidly as the diameter of the object approaches the distance between Finger 2 and Finger 3 (30 mm), resulting in more fingertip position changes and slips.

In particular, in the process of grasping a cylinderical object with a diameter of 60 mm, it seemed that the initial object was stably gripped, but slippage occurred over time. This implies that even if the initial grasp is stable, the grasping easily becomes unstable, and the object can be dropped even with a slight disturbance.

The gripper with w7-3 ARC joints firmly grasped the objects with diameter 50 mm and 60 mm, and the current values of each finger showed that they maintained grasping forces without slippage. However, slipping occurred with both grippers in the case of the 40 mm cylinder. Comparing the converged grasping postures, the w7-3 ARC joint enabled a more stable pinch grasping than the w7-6 ARC joint.

To estimate the maximum grasping force of two grippers when grasp cylinder-shape objects, a force sensor (OPTOFORCE, 3D Force sensor) was attached to the fingertip of Finger 1 (Fig. 4.13(a)). The maximum grasping force was defined as the fingertip force at the moment when grasping became unstable due to slippage occurred. Fig. 4.15 shows the results of maximum grasping force that each gripper can apply to a cylinder-shaped object using box-plot, and the circle points show 50 repeated grasps for each case. When grasp 50 mm
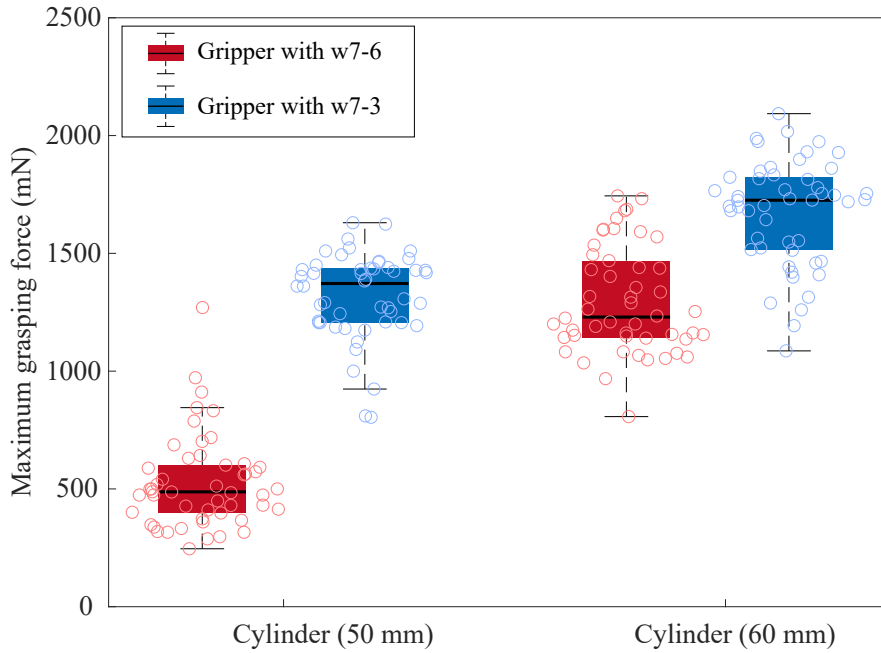
Figure 4.15: Maximum grasping force of two grippers grasping cylinders with 50 mm and 60 mm diameters

cylinder, the average maximum grasp force of gripper with w7-6 and w7-3 were 526 mN and 1320 mN, respectively, and grasping 60 mm cylinder, the average maximum grasp force of gripper with w7-6 and w7-3 were estimated 1297 mN and 1673 mN. On average, the gripper with w7-3 was able to produce a larger grasping force. However, depending on the position of the object and the grasping posture, the gripper with the w7-3 joint also showed slippage at the tip of the fingers at a low grasping force.

Chapter 5

CONCLUSIONS

In this study, the novel tendon-driven robotic finger structure was proposed. The proposed robotic finger was designed to unify the three mechanisms, *intrinsic/extrinsic actuator arrangement*, *ElaCVT-TSA*, and *ARC joint*. These new mechanisms mimic human musculoskeletal characteristics and improve the limitations of robotic hands that have been developed until now.

A tendon-driven robotic finger structure was proposed, based on the analysis of the fingertip velocity during various object-grasping motions performed by humans. In this proposed structure, the intrinsic actuators are responsible for slow motion, while an extrinsic actuator is utilized for motions that require both high force and speed. By separating the actuators, the robotic finger was able to achieve a more balanced shape through the optimized selection and arrangement of actuators.

ElaCVT-TSA, which combines the proposed ElaCVT and a TSA. Unlike conventional CVTs, which are large and heavy, ElaCVT can be manufactured

to be small and light and can be applied to small-size robotic applications like robotic hands. ElaCVT-TSA passively and continuously changes the reduction ratio depending on the external load applied at the end of the TSA and expands the operating region of the TSA. It was also found that the operating region of the ElaCVT-TSA could mimic the FV curves of muscles through experiments with various external loads. The ElaCVT has a cylindrical shape of 27 mm in length, and 24 mm in diameter, and weighs 12 g.

For the flexion/extension joints of the robotic finger, the Anthropomorphic rolling contact joint, a novel type of rolling contact joint, mimicking the tongue-and-groove mechanism and collateral ligaments of a human finger joint, was proposed. The ARC joint has the advantage of being simple and easy to manufacture and was applied after being reduced to a joint the size of a real human finger. In addition, it could be successfully integrated with multiple tendons passing around the joints. In the process of applying the ARC joint to the robotic finger, o-rings were applied to Ligament 2 instead of springs to reduce the volume of ARC joints. With elastic ligament and tongue-and-groove mechanism, the ARC joint is compliant, and the torsional stiffness of ARC joint passively increases according to the joint angle. The increment of torsional stiffness can be designed by adjusting the shape of the tongue and groove without additional weight and space. In addition, the ARC joint has a structure that can be completely disassembled and reassembled because it does not use adhesives or knots to fix the ligament, unlike the previous rolling contact joints, and thus is easy to maintain.

One of the applications that utilize the torsional stiffness increases as the joint is flexed is the robotic hand because the process of grasping consists of

two separate stages; searching and grasping. In the searching stage, the opened robotic hand (stretched fingers) with lower joint stiffness enables stable contact with objects and environments, and the high joint stiffness of the flexed fingers improves the grasping stability in the grasping stage. The torsional stiffness of six ARC joints was analyzed, and two three-finger grippers with different shapes of ARC joints were designed and fabricated to experimentally demonstrate that the ARC joint increases grasp stability in pinch grasping of small objects.

While the proposed robotic finger mimicked various characteristics of the human hand in order to enhance its performance, it also possesses limitations. Unlike a human finger, which is actuated by six muscles (three intrinsic muscles and three extrinsic muscles), the proposed robotic finger is actuated by only three actuators. As a result, the proposed robotic finger is limited in the following ways. Firstly, although the proximal interphalangeal (PIP) and distal interphalangeal (DIP) joints of the human finger are coupled while performing the natural motion, the DIP joint can be independently controlled in a limited range of motion, while the joint angles of PIP, DIP joints of the robotic finger are fixed at a 1:1 ratio. Secondly, the proposed robotic finger relies on the restoring force generated from the stretched ligament to extend the joints of the finger. However, the human finger can actively control the extension force using the extensor digitorum communis.

ElaCVT transmits power by using the friction generated between the lateral disc and the elastomer. Through a series of experiments, it was determined that the friction generated during operation causes wear on the elastomer, resulting in a shift in the position of the contact point between the lateral disc and the elastomer, which in turn increases the reduction ratio. This variation in the

reduction ratio leads to a decline in the overall performance of the ElaCVT system over time. To ensure high reliability and prolonged usage, it is necessary to periodically replace the elastomer. In order to facilitate easy replacement of the elastomer, improvements to the structure of the ElaCVT system are required. Additionally, further research on various elastomers composed of different materials is necessary to accurately determine the replacement cycle.

The proposed three mechanisms were successfully integrated into the robotic finger, which is of human-level size and weight, comprising three actuators. Furthermore, the modular structure of the proposed robotic finger allows for the potential for the manufacture of robotic hands in the future.

Bibliography

[1] M. J. Schreck, M. Kelly, S. Lander, A. Kaushik, H. Smith, S. Bell, V. Raman, D. Olles, J. Geigel, M. Olles, *et al.*, "Dynamic functional assessment of hand motion using an animation glove: The effect of stenosing tenosynovitis," *Hand*, vol. 13, no. 6, pp. 695–704, 2018.

[2] A. Chromy, L. Zalud, P. Dobsak, I. Suskevic, and V. Mrkvicova, "Limb volume measurements: comparison of accuracy and decisive parameters of the most used present methods," *Springerplus*, vol. 4, no. 1, pp. 1–15, 2015.

[3] P. De Leva, "Adjustments to zatsiorsky-seluyanov's segment inertia parameters," *Journal of biomechanics*, vol. 29, no. 9, pp. 1223–1230, 1996.

[4] D.-H. Lee, J.-H. Park, S.-W. Park, M.-H. Baeg, and J.-H. Bae, "Kitechhand: A highly dexterous and modularized robotic hand," *IEEE/ASME Transactions on Mechatronics*, vol. 22, no. 2, pp. 876–887, 2016.

[5] M. S. Johannes, J. D. Bigelow, J. M. Burck, S. D. Harshbarger, M. V. Kozlowski, and T. Van Doren, "An overview of the developmental process for the modular prosthetic limb," *Johns Hopkins APL Technical Digest*, vol. 30, no. 3, pp. 207–216, 2011.

[6] U. Kim, D. Jung, H. Jeong, J. Park, H.-M. Jung, J. Cheong, H. R. Choi, H. Do, and C. Park, "Integrated linkage-driven dexterous anthropomorphic robotic hand," *Nature communications*, vol. 12, no. 1, pp. 1–13, 2021.

[7] "Schunk svh 5-finger hand," https://schunk.com/us/en/gripping-systems/special-gripper/svh/c/PGR_3161, accessed: 2022-11-14.

[8] J. T. Belter, J. L. Segil, and B. SM, "Mechanical design and performance specifications of anthropomorphic prosthetic hands: a review," *Journal of rehabilitation research and development*, vol. 50, no. 5, p. 599, 2013.

[9] "Bebionic hand," https://www.ottobock.com/en-us/product/8E70, accessed: 2022-12-12.

[10] "i-limb," https://www.ossur.com/en-us/prosthetics/hands, accessed: 2022-12-12.

[11] "The shadow dextrous hand," http://www.shadow.org.uk/products/newhand.shtml, accessed: 2022-11-14.

[12] G. Palli, C. Melchiorri, G. Vassura, U. Scarcia, L. Moriello, G. Berselli, A. Cavallo, G. De Maria, C. Natale, S. Pirozzi, *et al.*, "The dexmart hand: Mechatronic design and experimental evaluation of synergy-based control for human-like grasping," *The International Journal of Robotics Research*, vol. 33, no. 5, pp. 799–824, 2014.

[13] Y.-J. Kim, J. Yoon, and Y.-W. Sim, "Fluid lubricated dexterous finger mechanism for human-like impact absorbing capability," *IEEE Robotics and Automation Letters*, vol. 4, no. 4, pp. 3971–3978, 2019.

[14] M. Grebenstein, A. Albu-Schäffer, T. Bahls, M. Chalon, O. Eiberger, W. Friedl, R. Gruber, S. Haddadin, U. Hagn, R. Haslinger, *et al.*, "The

dlr hand arm system," in *2011 IEEE International Conference on Robotics and Automation.* IEEE, 2011, pp. 3175–3182.

[15] J. Butterfaß, M. Grebenstein, H. Liu, and G. Hirzinger, "Dlr-hand ii: Next generation of a dextrous robot hand," in *Proceedings 2001 ICRA. IEEE International Conference on Robotics and Automation (Cat. No. 01CH37164)*, vol. 1. IEEE, 2001, pp. 109–114.

[16] C. Della Santina, C. Piazza, G. Grioli, M. G. Catalano, and A. Bicchi, "Toward dexterous manipulation with augmented adaptive synergies: The pisa/iit softhand 2," *IEEE Transactions on Robotics*, vol. 34, no. 5, pp. 1141–1156, 2018.

[17] W. S. You, Y. H. Lee, H. S. Oh, G. Kang, and H. R. Choi, "Design of a 3d-printable, robust anthropomorphic robot hand including intermetacarpal joints," *Intelligent Service Robotics*, vol. 12, no. 1, pp. 1–16, 2019.

[18] N. Feng, Q. Shi, H. Wang, J. Gong, C. Liu, and Z. Lu, "A soft robotic hand: design, analysis, semg control, and experiment," *The International Journal of Advanced Manufacturing Technology*, vol. 97, no. 1, pp. 319–333, 2018.

[19] J. Zhou, X. Chen, U. Chang, J.-T. Lu, C. C. Y. Leung, Y. Chen, Y. Hu, and Z. Wang, "A soft-robotic approach to anthropomorphic robotic hand dexterity," *Ieee Access*, vol. 7, pp. 101 483–101 495, 2019.

[20] R. Deimel and O. Brock, "A novel type of compliant and underactuated robotic hand for dexterous grasping," *The International Journal of Robotics Research*, vol. 35, no. 1-3, pp. 161–185, 2016.

[21] S. Abondance, C. B. Teeple, and R. J. Wood, "A dexterous soft robotic hand for delicate in-hand manipulation," *IEEE Robotics and Automation Letters*, vol. 5, no. 4, pp. 5502–5509, 2020.

[22] A. Schmitz, U. Pattacini, F. Nori, L. Natale, G. Metta, and G. Sandini, "Design, realization and sensorization of the dexterous icub hand," in *2010 10th IEEE-RAS International Conference on Humanoid Robots*. IEEE, 2010, pp. 186–191.

[23] L. B. Bridgwater, C. Ihrke, M. A. Diftler, M. E. Abdallah, N. A. Radford, J. Rogers, S. Yayathi, R. S. Askew, and D. M. Linn, "The robonaut 2 hand-designed to do work with tools," in *2012 IEEE International Conference on Robotics and Automation*. IEEE, 2012, pp. 3425–3430.

[24] H. D. P. C. A. Facilitate and N. Roots, "Upper extremity anatomy," *Fundamentals of Hand Therapy: Clinical Reasoning and Treatment Guidelines for Common Diagnoses of the Upper Extremity*, p. 22, 2007.

[25] R. L. Lieber, M. D. Jacobson, B. M. Fazeli, R. A. Abrams, and M. J. Botte, "Architecture of selected muscles of the arm and forearm: anatomy and implications for tendon transfer," *The Journal of hand surgery*, vol. 17, no. 5, pp. 787–798, 1992.

[26] M. D. Jacobson, R. Raab, B. M. Fazeli, R. A. Abrams, M. J. Botte, and R. L. Lieber, "Architectural design of the human intrinsic hand muscles," *The Journal of hand surgery*, vol. 17, no. 5, pp. 804–809, 1992.

[27] M. Millard, T. Uchida, A. Seth, and S. L. Delp, "Flexing computational muscle: modeling and simulation of musculotendon dynamics," *Journal of biomechanical engineering*, vol. 135, no. 2, 2013.

[28] K.-N. An, E. Y. Chao, W. P. Cooney III, and R. L. Linscheid, "Normative model of human hand for biomechanical analysis," *Journal of biomechanics*, vol. 12, no. 10, pp. 775–788, 1979.

[29] S. W. Lee, H. Chen, J. D. Towles, and D. G. Kamper, "Estimation of the effective static moment arms of the tendons in the index finger extensor mechanism," *Journal of biomechanics*, vol. 41, no. 7, pp. 1567–1573, 2008.

[30] J. H. Lee, D. S. Asakawa, J. T. Dennerlein, and D. L. Jindrich, "Finger muscle attachments for an opensim upper-extremity model," *PloS one*, vol. 10, no. 4, p. e0121712, 2015.

[31] C. Della Santina, M. Bianchi, G. Averta, S. Ciotti, V. Arapi, S. Fani, E. Battaglia, M. G. Catalano, M. Santello, and A. Bicchi, "Postural hand synergies during environmental constraint exploitation," *Frontiers in neurorobotics*, vol. 11, p. 41, 2017.

[32] J. Biggs and K. Horch, "A three-dimensional kinematic model of the human long finger and the muscles that actuate it," *Medical engineering & physics*, vol. 21, no. 9, pp. 625–639, 1999.

[33] A. Mueller, "Modern robotics: Mechanics, planning, and control [bookshelf]," *IEEE Control Systems Magazine*, vol. 39, no. 6, pp. 100–102, 2019.

[34] P. Hahn, H. Krimmer, A. Hradetzky, and U. Lanz, "Quantitative analysis of the linkage between the interphalangeal joints of the index finger: An in vivo study," *Journal of Hand Surgery*, vol. 20, no. 5, pp. 696–699, 1995.

[35] K. J. Van-Zwieten, K. P. Schmidt, G. J. Bex, P. L. Lippens, and W. Duyvendak, "An analytical expression for the dip–pip flexion inter-

dependence in human fingers," *Acta of Bioengineering and Biomechanics*, vol. 17, no. 1, pp. 129–135, 2015.

[36] G. P. Kontoudis, M. Liarokapis, K. G. Vamvoudakis, and T. Furukawa, "An adaptive actuation mechanism for anthropomorphic robot hands," *Frontiers in Robotics and AI*, vol. 6, p. 47, 2019.

[37] S. H. Jeong, K.-S. Kim, and S. Kim, "Development of a robotic finger with an active dual-mode twisting actuation and a miniature tendon tension sensor," in *2016 IEEE International Conference on Advanced Intelligent Mechatronics (AIM)*. IEEE, 2016, pp. 1–6.

[38] A. Mottard, T. Laliberté, and C. Gosselin, "Underactuated tendon-driven robotic/prosthetic hands: Design issues." in *Robotics: Science and Systems*, vol. 7, 2017.

[39] K.-N. An, Y. Ueba, E. Chao, W. Cooney, and R. Linscheid, "Tendon excursion and moment arm of index finger muscles," *Journal of biomechanics*, vol. 16, no. 6, pp. 419–425, 1983.

[40] K. Andrianesis and A. Tzes, "Development and control of a multifunctional prosthetic hand with shape memory alloy actuators," *Journal of Intelligent & Robotic Systems*, vol. 78, no. 2, pp. 257–289, 2015.

[41] A. A. M. Faudzi, J. Ooga, T. Goto, M. Takeichi, and K. Suzumori, "Index finger of a human-like robotic hand using thin soft muscles," *IEEE Robotics and Automation Letters*, vol. 3, no. 1, pp. 92–99, 2017.

[42] V. Wall, G. Zöller, and O. Brock, "A method for sensorizing soft actuators and its application to the rbo hand 2," in *2017 IEEE International Conference on Robotics and Automation (ICRA)*. IEEE, 2017, pp. 4965–4970.

[43] J. Hughes, U. Culha, F. Giardina, F. Guenther, A. Rosendo, and F. Iida, "Soft manipulators and grippers: a review," *Frontiers in Robotics and AI*, vol. 3, p. 69, 2016.

[44] C. Piazza, G. Grioli, M. Catalano, and A. Bicchi, "A century of robotic hands," *Annual Review of Control, Robotics, and Autonomous Systems*, vol. 2, pp. 1–32, 2019.

[45] J. Zhang, J. Sheng, C. T. O'Neill, C. J. Walsh, R. J. Wood, J.-H. Ryu, J. P. Desai, and M. C. Yip, "Robotic artificial muscles: Current progress and future perspectives," *IEEE Transactions on Robotics*, vol. 35, no. 3, pp. 761–781, 2019.

[46] J. D. Madden, N. A. Vandesteeg, P. A. Anquetil, P. G. Madden, A. Takshi, R. Z. Pytel, S. R. Lafontaine, P. A. Wieringa, and I. W. Hunter, "Artificial muscle technology: physical principles and naval prospects," *IEEE Journal of oceanic engineering*, vol. 29, no. 3, pp. 706–728, 2004.

[47] R. J. Schwarz and C. Taylor, "The anatomy and mechanics of the human hand," *Artificial limbs*, vol. 2, no. 2, pp. 22–35, 1955.

[48] E. Azizi, E. L. Brainerd, and T. J. Roberts, "Variable gearing in pennate muscles," *Proceedings of the National Academy of Sciences*, vol. 105, no. 5, pp. 1745–1750, 2008.

[49] G. Palli, C. Natale, C. May, C. Melchiorri, and T. Wurtz, "Modeling and control of the twisted string actuation system," *IEEE/ASME Transactions on Mechatronics*, vol. 18, no. 2, pp. 664–673, 2012.

[50] I. Gaponov, D. Popov, and J.-H. Ryu, "Twisted string actuation systems: A study of the mathematical model and a comparison of twisted strings,"

IEEE/ASME Transactions on Mechatronics, vol. 19, no. 4, pp. 1331–1342, 2013.

[51] S. H. Jeong and K.-S. Kim, "A 2-speed small transmission mechanism based on twisted string actuation and a dog clutch," *IEEE Robotics and Automation Letters*, vol. 3, no. 3, pp. 1338–1345, 2018.

[52] H. Singh, D. Popov, I. Gaponov, and J.-H. Ryu, "Twisted string-based passively variable transmission: Concept, model, and evaluation," *Mechanism and Machine Theory*, vol. 100, pp. 205–221, 2016.

[53] A. V. Hill, "The heat of shortening and the dynamic constants of muscle," *Proceedings of the Royal Society of London. Series B-Biological Sciences*, vol. 126, no. 843, pp. 136–195, 1938.

[54] R. Close, "Dynamic properties of mammalian skeletal muscles." *Physiological reviews*, vol. 52, no. 1, pp. 129–197, 1972.

[55] M. Bonilla, E. Farnioli, C. Piazza, M. Catalano, G. Grioli, M. Garabini, M. Gabiccini, and A. Bicchi, "Grasping with soft hands," in *2014 IEEE-RAS International Conference on Humanoid Robots.* IEEE, 2014, pp. 581–587.

[56] M. Manti, T. Hassan, G. Passetti, N. D'Elia, C. Laschi, and M. Cianchetti, "A bioinspired soft robotic gripper for adaptable and effective grasping," *Soft Robotics*, vol. 2, no. 3, pp. 107–116, 2015.

[57] J. Zhou, S. Chen, and Z. Wang, "A soft-robotic gripper with enhanced object adaptation and grasping reliability," *IEEE Robotics and automation letters*, vol. 2, no. 4, pp. 2287–2293, 2017.

[58] C. B. Teeple, T. N. Koutros, M. A. Graule, and R. J. Wood, "Multi-segment soft robotic fingers enable robust precision grasping," *The International Journal of Robotics Research*, vol. 39, no. 14, pp. 1647–1667, 2020.

[59] H. Liu, K. Xu, B. Siciliano, and F. Ficuciello, "The mero hand: A mechanically robust anthropomorphic prosthetic hand using novel compliant rolling contact joint," in *2019 IEEE/ASME International Conference on Advanced Intelligent Mechatronics (AIM)*. IEEE, 2019, pp. 126–132.

[60] C. L. Collins, "Kinematics of robot fingers with circular rolling contact joints," *Journal of Robotic Systems*, vol. 20, no. 6, pp. 285–296, 2003.

[61] Y. Zhu, G. Wei, L. Ren, Z. Luo, and J. Shang, "An anthropomorphic robotic finger with innate human-finger-like biomechanical advantages part i: Design, ligamentous joint, and extensor mechanism," *IEEE Transactions on Robotics*, 2022.

[62] Y. Zhu, G. Wei, L. Ren, Z. Luo, and J. Shang, "An anthropomorphic robotic finger with innate human-finger-like biomechanical advantages part ii: flexible tendon sheath and grasping demonstration," *IEEE Transactions on Robotics*, 2022.

[63] Z. Xu, E. Todorov, B. Dellon, and Y. Matsuoka, "Design and analysis of an artificial finger joint for anthropomorphic robotic hands," in *2011 IEEE International Conference on Robotics and Automation*. IEEE, 2011, pp. 5096–5102.

[64] Z. Xu and E. Todorov, "Design of a highly biomimetic anthropomorphic robotic hand towards artificial limb regeneration," in *2016 IEEE Interna-*

tional Conference on Robotics and Automation (ICRA). IEEE, 2016, pp. 3485–3492.

[65] B. M. Hillberry and A. S. Hall Jr, "Rolling contact joint," Jan. 13 1976, uS Patent 3,932,045.

[66] S.-H. Kim, H. In, J.-R. Song, and K.-J. Cho, "Force characteristics of rolling contact joint for compact structure," in *2016 6th IEEE International Conference on Biomedical Robotics and Biomechatronics (BioRob).* IEEE, 2016, pp. 1207–1212.

[67] S. W. Hong, J. Yoon, Y.-J. Kim, and H. S. Gong, "Novel implant design of the proximal interphalangeal joint using an optimized rolling contact joint mechanism," *Journal of Orthopaedic Surgery and Research*, vol. 14, no. 1, pp. 1–13, 2019.

[68] R. Liang, G. Xu, Q. Zhang, K. Jiang, M. Li, and B. He, "Design and characterization of a rolling-contact involute joint and its applications in finger exoskeletons," *Machines*, vol. 10, no. 5, p. 301, 2022.

[69] D. Zhang, Y. Sun, and T. C. Lueth, "Design of a novel tendon-driven manipulator structure based on monolithic compliant rolling-contact joint for minimally invasive surgery," *International Journal of Computer Assisted Radiology and Surgery*, vol. 16, no. 9, pp. 1615–1625, 2021.

[70] A. Minami, K.-N. An, W. P. Cooney III, R. L. Linscheid, and E. Y. Chao, "Ligament stability of the metacarpophalangeal joint: a biomechanical study," *The Journal of hand surgery*, vol. 10, no. 2, pp. 255–260, 1985.

[71] S. Kamnerdnakta, H. E. Huetteman, and K. C. Chung, "Complications of proximal interphalangeal joint injuries: prevention and treatment," *Hand clinics*, vol. 34, no. 2, pp. 267–288, 2018.

[72] C. Dumont, G. Albus, D. Kubein-Meesenburg, J. Fanghänel, K. M. Stürmer, and H. Nägerl, "Morphology of the interphalangeal joint surface and its functional relevance," *The Journal of hand surgery*, vol. 33, no. 1, pp. 9–18, 2008.

초 록

엔드이팩터는 로봇과 주변 환경이 상호작용하는 통로로 매니퓰레이터가 수행할 수 있는 작업은 엔드이펙터의 성능에 제한된다. 사람 중심의 환경에 로봇이 적용되어 사람 수준의 다양한 작업을 수행하기 위해서는 사람 손 수준의 성능을 갖는 로봇 손이 필수적이며 사람 손 수준의 성능은 단순히 힘-속도, 자유도만을 포함하는 것이 아닌 크기와 무게 그리고 물체 조작에 도움을 주는 여러 손 특성도 포함한다. 그러나 현재까지 사람 손 수준의 무게, 크기, 힘 그리고 자유도를 모두 만족시키는 로봇 손은 개발되지 않았으며 여전히 도전적인 과제로 남아있다. 본 논문에서는 로봇 손가락의 성능을 향상하기 위하여 사람의 근골격 특성을 반영한 세 가지의 새로운 메커니즘을 제안하고 이를 통합한 모듈형 로봇 손가락 구조를 보인다.

첫 번째로, 사람의 손 근육 배치와 유사한 내재/외재 구동기 배치를 적용한 힘줄 구동 로봇 손가락 구조를 제안하고 분석한다. 로봇 손가락은 다섯 개의 서로 다른 힘줄과 인대로 구성된다. 사람 손동작 분석에 기반하여 로봇 손가락의 구동기는 느린 속도를 담당하는 내재 구동기와 빠르고 큰 힘이 모두 요구되는 외재 구동기로 구분된다.

두 번째로, 구동기의 크기와 무게를 유지하며 성능을 향상하기 위하여 새로운 개념의 무단 변속기 Elastomeric Continuously Variable Transmission (ElaCVT)

을 제안하고 이를 로봇 손가락의 외재 구동기에 적용하였다. ElaCVT는 선형 구동기의 작동 영역을 확장하고 출력단에 가해지는 외부 하중에 따라 감속비를 수동적으로 변경하여 근육의 힘-속도 곡선을 모사할 수 있다. 본 연구에서는 근육의 특성을 모사하기 위해 선형 액추에이터로 ElaCVT에 줄 꼬임 메커니즘을 적용한 ElaCVT-TSA를 제안, 근육의 동작 영역을 모사할 수 있음을 보였다.

마지막으로 로봇 손가락의 모든 굽힘/펼침 관절에 적용된 사람의 관절구조를 모사한 유연 구름 접촉 관절 (Anthropomorphic Rolling Contact joint)을 제안한다. Anthropomorphic rolling contact joint는 사람 관절의 tongue-and-groove 형상과 collateral ligament를 모사하여 관절의 안정성을 향상시켰다. 기존의 유연 관절과 달리 관절이 펴진 상태에서는 유연한 상태를 유지하며 굽혀진 상태에서는 강성이 증가한다는 특징을 갖는다. 특히, 강성 변화에 별도의 구동기가 요구되지 않아 기존의 관절에서 무게, 크기 증가 없이 해당 특징 구현이 가능하다. 이는 로봇 손가락에 적용되어 손가락을 펴고 물체를 탐색하는 과정에서는 충격을 흡수하여 안정적인 접촉을 구현할 수 있으며 물체를 파지하는 과정에서는 손가락을 굽혀 강인하게 물체를 파지할 수 있게 한다. Anthropomorphic rolling contact joint를 적용한 그립퍼를 이용하여 제안하는 가변 강성 유연 관절이 pinch grasping의 파지 안정성을 높임을 보였다.

주요어: 로봇 손, 무단 변속기, 유연 관절, 생체 모방

학번: 2015-26106